device (Millipore, Billerica, MA, USA), and protein concentrations were estimated using a Coomassie Plus Protein Assay kit (Thermo Fisher Scientific, Rockford, IL).

2.5. Flow cytometric analysis

MDA-MB-435 or MDA-MB-435^{EphA10} (5×10^5 cells) were suspended in Suspension buffer (2% FBS containing PBS) and incubated with 20 μg diabody or 2 μg control IgG (anti-EphA10, anti-CD3) for 1 h on ice, respectively. After washing with Suspension buffer, the cells were incubated with Surelight P3 (614 nm excitation and 662 nm emission) labeled antibodies against the His tag (Columbia Biosciences, Frederick, MD) and Surelight P3 labeled antibodies against the mouse IgG (Columbia Biosciences) for 1 h on ice. The cells were washed again and resuspended in 500 μL Suspension buffer and flow cytometric analysis was performed (FACScanto; BD Biosciences, San Jose, CA). All tests were carried out in triplicate.

2.6. Cytotoxicity assays

Cytotoxicity assays were performed as described previously with slight modifications [14]. In brief, MDA-MB-435^{EphA10} cells and MDA-MB-435 parent cells as target cells (10^3 cells/well) were added to 96-well plates with 10% FBS containing D-MEM at 37 °C in a humidified atmosphere containing 5% CO_2. After overnight culture, supernatants were removed and non-stimulated human PBMC from healthy donors as effector cells were added to an effector-to-target (E/T) ratio of 10 with each of the antibodies (0.1–10 μg/mL), respectively. After 48 h of incubation, lactate dehydrogenase (LDH) released into the supernatant was measured using a CytoTox 96® non-radioactive cytotoxicity assay (Promega, Madison, WI). Percentages of specific lysis were calculated according to the formula: % cytotoxicity = [(experimental release) – (effector spontaneous release) – (target spontaneous release)]/[(target maximum release) – (target spontaneous release)] × 100. All tests were carried out in triplicate.

2.7. Statistical analysis

Differences in cytotoxicity assay results between the control and target groups were compared using the unpaired Student's *t*-test.

3. Result and discussion

3.1. Formulations of diabody binding to EphA10 and CD3

A BsAb was constructed using two different scFv fragments (scFv A and scFv B) derived from the anti-EphA10 IgG and anti-CD3 IgG. His-tagged and FLAG-tagged VL-VH chain (EphA10-VL-Linker-CD3-VH; scFv A and CD3-VL-Linker- EphA10-VH; scFv

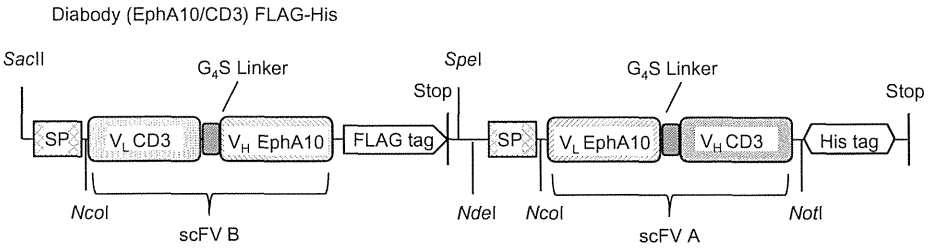

Fig. 1. Construction of the diabody-expressing vector.

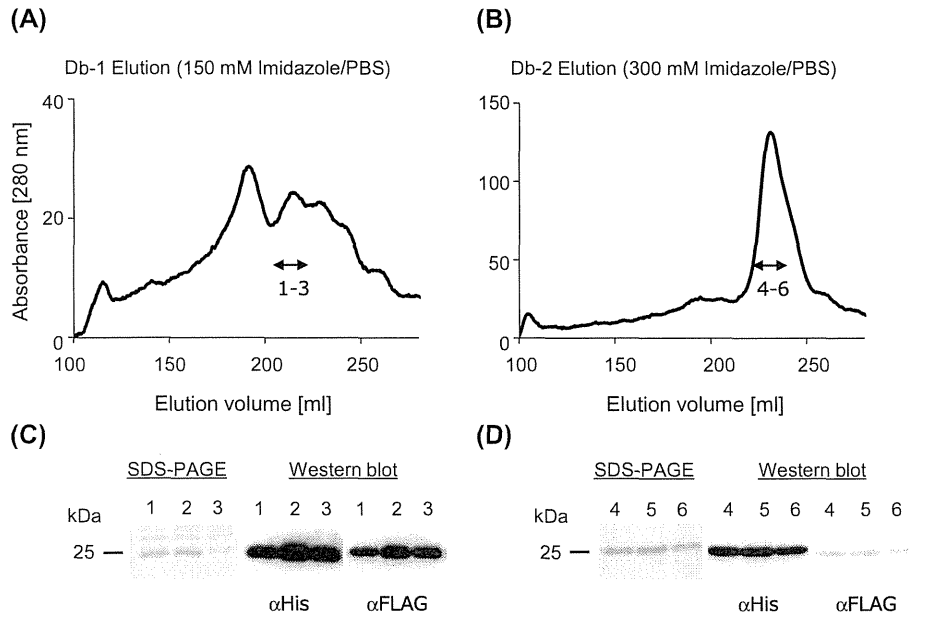

Fig. 2. Characteristics of diabody (Db-1 and Db-2). Gel filtration chromatography profile of diabodies, which were purified by IMAC. (A) 150 mM imidazole elution pattern (Db-1 as heterodimer) and (B) 300 mM imidazole elution pattern (Db-2 as homodimer). SDS–PAGE and Western blot analysis of dimeric Db-1 (C) and Db-2 (D). The line indicates the apparent molecular weight (25 kDa).

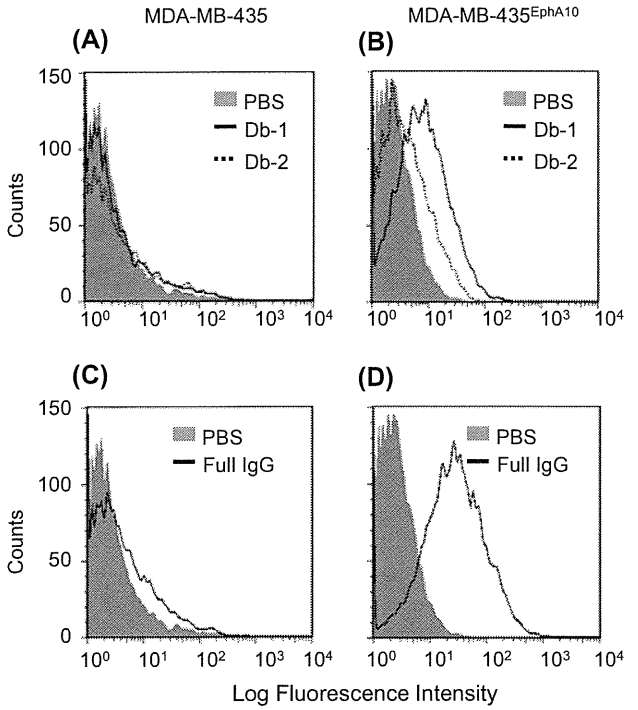

Fig. 3. Binding activity of diabody against EphA10-transfected cells and the parent cells (MDA-MD-435). The left panels (A, C) show the binding ability of the diabodies (A) and of the full IgG (C) against parental cells (MDA-MB-435) and the right panels (B, D) are against EphA10-transfeted cells. Binding activities were measured using 20 μg of each diabody sample. Cell-binding proteins were detected using SureLight P3 conjugated anti-His tag or anti-mouse IgG mAb. Filled bars are vehicle control (PBS).

B, respectively) were constructed (Fig. 1). The plasmid vector construct was designed by adding an N-terminal signal peptide to express BsAb in a soluble form and adding a C-terminal hexahistidine (His × 6) tag or FLAG tag to allow purification by affinity chromatography on a Ni-Sepharose column. This plasmid vector was transfected into BL21 (DE3) Star *E. coli* cells. Pooled supernatants were purified by IMAC using two elution buffers, and fractions containing the diabody further purified by gel-filtration chromatography (Fig. 2A and B). SDS–PAGE under reducing conditions followed by Western blot analysis showed only a single band indicating a ~25 kDa protein (Fig. 2C and D), consistent with the calculated molecular mass of approximately 25 kDa for each scFv. Because these two scFv chains are structured as homodimers, they would be expected to show only low binding activity compared with the heterodimeric form that can fully recognize the target molecules. Therefore, the diabody formulation was checked by western blot against both an anti-His and an anti-FLAG antibody (Fig. 2C and D). These results showed that the diabody existed as heterodimer in the condition of 150 mM imidazole elution, because the amounts of His- and FLAG-tagged scFvs were similar (Fig. 2C). However, the fraction eluted by 300 mM imidazole was primarily composed of homodimers, because the anti-His-tag staining was much stronger than the anti-FLAG tag staining (Fig. 2D). Because His-tagged homodimer antibodies would get trapped strongly by a Ni-Sepharose column, two concentrations of imidazole were used to elute the scFvs (Db-1: 150 mM imidazole/PBS, Db-2: 300 mM imidazole/PBS). The heterodimers indeed were eluted at a lower imidazole concentration than the homodimers.

3.2. Binding activity of diabody for human EphA10

Binding activities of these diabodies (Db-1 and Db-2) were examined by flow cytometric analysis using the MDA-MB-435 parental cells, MDA-MB-435^{EphA10} cells. Specific binding of EphA10 antigens to both Db-1 and Db-2 was observed (Fig. 3). Interestingly, the binding activity of diabody Db-1 was stronger than that of Db-2. These results indicated that the binding activity of the homodimer was reduced because this formulation would have mismatches between each VL and VH. Furthermore, the structural difference between homodimers and heterodimers had a significant effect on the binding activity.

3.3. Redirected target cell lysis of diabody with PBMC

The efficacy of T-cell mediated redirected lysis of MDA-MB-435^{EphA10} cells and the parental cells following addition of each diabody was examined using an LDH cytotoxicity assay. Non-stimulated PBMC were used as effector cells at E/T ratios of 10, respectively. As shown in Fig. 4, the Db-1 and Db-2 diabodies showed dose-dependent cytotoxic activity against MDA-MB-435^{EphA10} cells compared with the scFv constructs (anti-EphA10 scFV). Furthermore, the cytotoxic efficacy of Db-1 was higher than that of Db-2 at low antibody concentrations, indicating that the heterodimer would increase the cytotoxicity related to binding of the antigen.

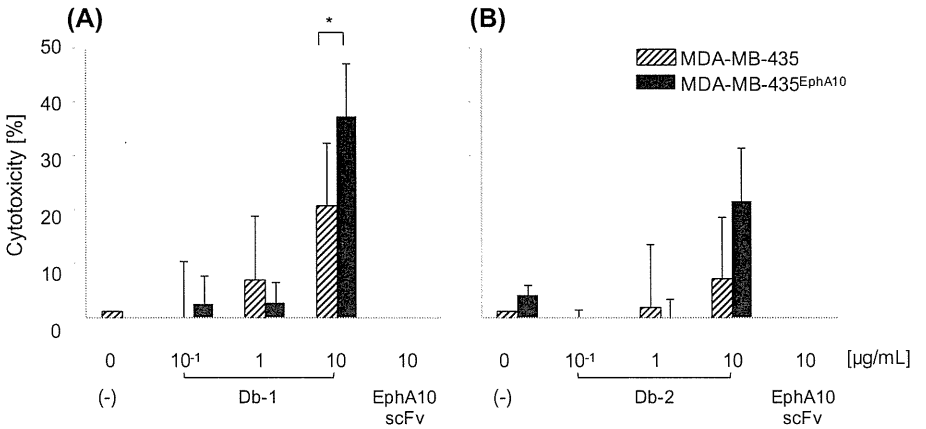

Fig. 4. *In vitro* cytotoxicity of diabody formulations (Db-1 and Db-2) against MDA-MB-435^{EphA10} and parental cells. The left panels are heterodimeric diabody, Db-1 (A) and the right panels are homodimeric diabody, Db-2 (B). MDA-MB-435 parental cells (slashed column) and MDA-MB-435^{EphA10} (black column) cells were co-cultured respectively with human PBMC at E/T ratios of 10. Each point represents the mean of triplicate determinations; error bars represent the standard deviations of triplicate determinations. Asterisks label readings that were statistically significant (unpaired Student's *t*-test) from MDA-MB-435 and MDA-MB-435^{EphA10} ($^*P \leqslant 0.05$).

The results of this study demonstrate that heterodimeric diabodies can show potent binding activity and specificity against cells that express the target antigen. Purified heterodimeric diabody formulations would lead to higher activity because of their increased affinity against two antigens, compared to homodimers or mixtures of homodimers plus heterodimers. Therefore, it is necessary to optimize purification protocols using HPLC etc. However, diabody formulations consisting of two chains of VL and VH could in principle form several types of mixed species. Thus, the protocols for bispecific antibodies should be optimized to produce a formulation containing a single species, e.g. by using linkers to produce a single chain diabody or tandem scFV. This should improve and standardize the desired binding functions of the BsAbs. The construction of such modified antibodies, e.g. scDb and faFV, shows great potential for the development of novel therapeutic drugs.

Acknowledgment

This work was supported by JSPS KAKENHI Grant Number 24680093.

References

[1] H.C. Aasheim, S. Patzke, H.S. Hjorthaug, E.F. Finne, Characterization of a novel Eph receptor tyrosine kinase, EphA10, expressed in testis, Biochim. Biophys. Acta 1723 (2005) 1–7.

[2] L. Truitt, A. Freywald, Dancing with the dead: Eph receptors and their kinase-null partners, Biochem. Cell Biol. 89 (2011) 115–129.

[3] K. Nagano, T. Yamashita, M. Inoue, K. Higashisaka, Y. Yoshioka, Y. Abe, Y. Mukai, H. Kamada, Y. Tsutsumi, S. Tsunoda, Eph receptor A10 has a potential as a target for a prostate cancer therapy, Biochem. Biophys. Res. Commun. 450 (2014) 545–549.

[4] K. Nagano, S. Kanasaki, T. Yamashita, Y. Maeda, M. Inoue, K. Higashisaka, Y. Yoshioka, Y. Abe, Y. Mukai, H. Kamada, Y. Tsutsumi, S. Tsunoda, Expression of Eph receptor A10 is correlated with lymph node metastasis and stage progression in breast cancer patients, Cancer Med. 2 (2013) 972–977.

[5] K. Nagano, Y. Maeda, S. Kanasaki, T. Watanabe, T. Yamashita, M. Inoue, K. Higashisaka, Y. Yoshioka, Y. Abe, Y. Mukai, H. Kamada, Y. Tsutsumi, S. Tsunoda, Ephrin receptor A10 is a promising drug target potentially useful for breast cancers including triple negative breast cancers, J. Control. Release 189 (2014) 72–79.

[6] D. Schrama, R.A. Reisfeld, J.C. Becker, Antibody targeted drugs as cancer therapeutics, Nat. Rev. Drug Discovery 5 (2006) 147–159.

[7] M.K. Gleason, J.A. Ross, E.D. Warlick, T.C. Lund, M.R. Verneris, A. Wiernik, S. Spellman, M.D. Haagenson, A.J. Lenvik, M.R. Litzow, P.K. Epling-Burnette, B.R. Blazar, L.M. Weiner, D.J. Weisdorf, D.A. Vallera, J.S. Miller, CD16xCD33 bispecific killer cell engager (BiKE) activates NK cells against primary MDS and MDSC CD33+ targets, Blood 123 (2014) 3016–3026.

[8] C. Somasundaram, R. Arch, S. Matzku, M. Zoller, Development of a bispecific F(ab')2 conjugate against the complement receptor CR3 of macrophages and a variant CD44 antigen of rat pancreatic adenocarcinoma for redirecting macrophage-mediated tumor cytotoxicity, Cancer Immunol. Immunother. 42 (1996) 343–350.

[9] S.R. Frankel, P.A. Baeuerle, Targeting T cells to tumor cells using bispecific antibodies, Curr. Opin. Chem. Biol. 17 (2013) 385–392.

[10] I. Shimomura, S. Konno, A. Ito, Y. Masakari, R. Orimo, S. Taki, K. Arai, H. Ogata, M. Okada, S. Furumoto, M. Onitsuka, T. Omasa, H. Hayashi, Y. Katayose, M. Unno, T. Kudo, M. Umetsu, I. Kumagai, R. Asano, Rearranging the domain order of a diabody-based IgG-like bispecific antibody enhances its antitumor activity and improves its degradation resistance and pharmacokinetics, MAbs 6 (2014).

[11] R. Asano, T. Kumagai, K. Nagai, S. Taki, I. Shimomura, K. Arai, H. Ogata, M. Okada, F. Hayasaka, H. Sanada, T. Nakanishi, T. Karvonen, H. Hayashi, Y. Katayose, M. Unno, T. Kudo, M. Umetsu, I. Kumagai, Domain order of a bispecific diabody dramatically enhances its antitumor activity beyond structural format conversion: the case of the hEx3 diabody, Protein Eng. Des. Sel. 26 (2013) 359–367.

[12] R. Asano, K. Ikoma, I. Shimomura, S. Taki, T. Nakanishi, M. Umetsu, I. Kumagai, Cytotoxic enhancement of a bispecific diabody by format conversion to tandem single-chain variable fragment (taFv): the case of the hEx3 diabody, J. Biol. Chem. 286 (2011) 1812–1818.

[13] R. Asano, K. Ikoma, Y. Sone, H. Kawaguchi, S. Taki, H. Hayashi, T. Nakanishi, M. Umetsu, Y. Katayose, M. Unno, T. Kudo, I. Kumagai, Highly enhanced cytotoxicity of a dimeric bispecific diabody, the hEx3 tetrabody, J. Biol. Chem. 285 (2010) 20844–20849.

[14] A. Loffler, P. Kufer, R. Lutterbuse, F. Zettl, P.T. Daniel, J.M. Schwenkenbecher, G. Riethmuller, B. Dorken, R.C. Bargou, A recombinant bispecific single-chain antibody, CD19 × CD3, induces rapid and high lymphoma-directed cytotoxicity by unstimulated T lymphocytes, Blood 95 (2000) 2098–2103.

nature
structural &
molecular biology

Structural basis of starvation-induced assembly of the autophagy initiation complex

Yuko Fujioka[1,8], Sho W Suzuki[2,3,8], Hayashi Yamamoto[2,8], Chika Kondo-Kakuta[2], Yayoi Kimura[4], Hisashi Hirano[4], Rinji Akada[5], Fuyuhiko Inagaki[6,7], Yoshinori Ohsumi[2] & Nobuo N Noda[1,7]

Assembly of the preautophagosomal structure (PAS) is essential for autophagy initiation in yeast. Starvation-induced dephosphorylation of Atg13 is required for the formation of the Atg1–Atg13–Atg17–Atg29–Atg31 complex (Atg1 complex), a prerequisite for PAS assembly. However, molecular details underlying these events have not been established. Here we studied the interactions of yeast Atg13 with Atg1 and Atg17 by X-ray crystallography. Atg13 binds tandem microtubule interacting and transport domains in Atg1, using an elongated helix-loop-helix region. Atg13 also binds Atg17, using a short region, thereby bridging Atg1 and Atg17 and leading to Atg1-complex formation. Dephosphorylation of specific serines in Atg13 enhanced its interaction with not only Atg1 but also Atg17. These observations update the autophagy-initiation model as follows: upon starvation, dephosphorylated Atg13 binds both Atg1 and Atg17, and this promotes PAS assembly and autophagy progression.

Autophagy is an intracellular degradation system conserved among eukaryotes. It has various physiological roles in the recycling of intracellular components such as proteins and organelles[1]. The hallmark of autophagy is the formation of a double membrane–bound structure, the autophagosome, that sequesters cytoplasmic materials and delivers them to the lytic compartment, i.e., the lysosome or vacuole, for degradation[2]. Autophagosome formation involves remarkable membrane dynamics mechanistically distinct from conventional membrane traffic, but the molecular mechanism of this process remains unclear.

Genetic analyses in the budding yeast *Saccharomyces cerevisiae* enabled us to identify 18 autophagy-related (Atg) proteins essential for autophagosome formation[2]. Most of these Atg proteins localize to the PAS proximal to the vacuole[3,4]. The PAS then generates an isolation membrane, the precursor of an autophagosome. Therefore, uncovering the structure and function of the PAS is essential for understanding the molecular mechanism of autophagosome formation.

Autophagy is strongly induced upon starvation, which is itself regulated by the nutrient sensor Tor kinase complex 1 (TORC1) and its substrate Atg13 (refs. 5–7). Atg13 is hyperphosphorylated by TORC1 under nutrient-rich conditions. When TORC1 activity is inhibited upon starvation, Atg13 is rapidly dephosphorylated, and this initiates the assembly of the PAS and consequently autophagosome formation. We previously reported that Atg13 interacts with Atg1, the only identified protein kinase essential for autophagy, and the Atg1–Atg13 complex further interacts with Atg17–Atg29–Atg31, the constitutively formed PAS-scaffold subcomplex, in a starvation-dependent manner[7,8]. These interactions lead to the formation of the Atg1–Atg13–Atg17–Atg29–Atg31 complex (Atg1 complex; ULK1 complex in mammals)[9,10]. This complex functions as a scaffold for the PAS and recruits downstream Atg proteins to the PAS, to initiate autophagosome formation. We previously proposed a model wherein, upon starvation, dephosphorylation of Atg13 increases its affinity with Atg1, and this in turn triggers PAS assembly[7]. This interaction enhances the activity of Atg1 kinase, and this enhanced kinase activity is also crucial for autophagy progression[7]. However, the structural basis of these events in autophagy initiation has not been well established. Moreover, a recent study presented a contradictory result that Atg13 constitutively forms a complex with Atg1 and that phosphorylated Atg13 does not regulate the formation of the Atg1 complex[11]. Thus, the molecular mechanisms of Atg13-mediated PAS assembly and its regulation remain critical issues that need to be addressed.

Here, we set out to reveal the molecular basis of autophagy initiation by starvation. We first identified the Atg1-binding and Atg17-binding regions of Atg13 and then determined the structural basis of the interactions of Atg13 with Atg1 and Atg17 by X-ray crystallography. Mutational studies both *in vitro* and *in vivo* revealed how dephosphorylation of specific serine residues enhances the interaction of Atg13 with Atg1 and Atg17 and consequently initiates the PAS assembly and autophagy.

RESULTS

Identification of the minimum Atg1-binding domain of Atg13

Atg13 interacts with both Atg1 and Atg17 (refs. 7,12,13), the key components of the Atg1 complex. Thus, structural information on

[1]Institute of Microbial Chemistry (BIKAKEN), Tokyo, Japan. [2]Frontier Research Center, Tokyo Institute of Technology, Yokohama, Japan. [3]Graduate School of Bioscience and Biotechnology, Tokyo Institute of Technology, Yokohama, Japan. [4]Graduate School of Medical Life Science and Advanced Medical Research Center, Yokohama City University, Yokohama, Japan. [5]Department of Applied Molecular Bioscience, Graduate School of Medicine, Yamaguchi University, Ube, Japan. [6]Department of Structural Biology, Faculty of Advanced Life Science, Hokkaido University, Sapporo, Japan. [7]Core Research for Evolutionary Science and Technology (CREST), Japan Science and Technology Agency, Tokyo, Japan. [8]These authors contributed equally to this work. Correspondence should be addressed to N.N.N. (nn@bikaken.or.jp) or Y.O. (yohsumi@iri.titech.ac.jp).

Received 11 October 2013; accepted 7 April 2014; published online 4 May 2014; doi:10.1038/nsmb.2822

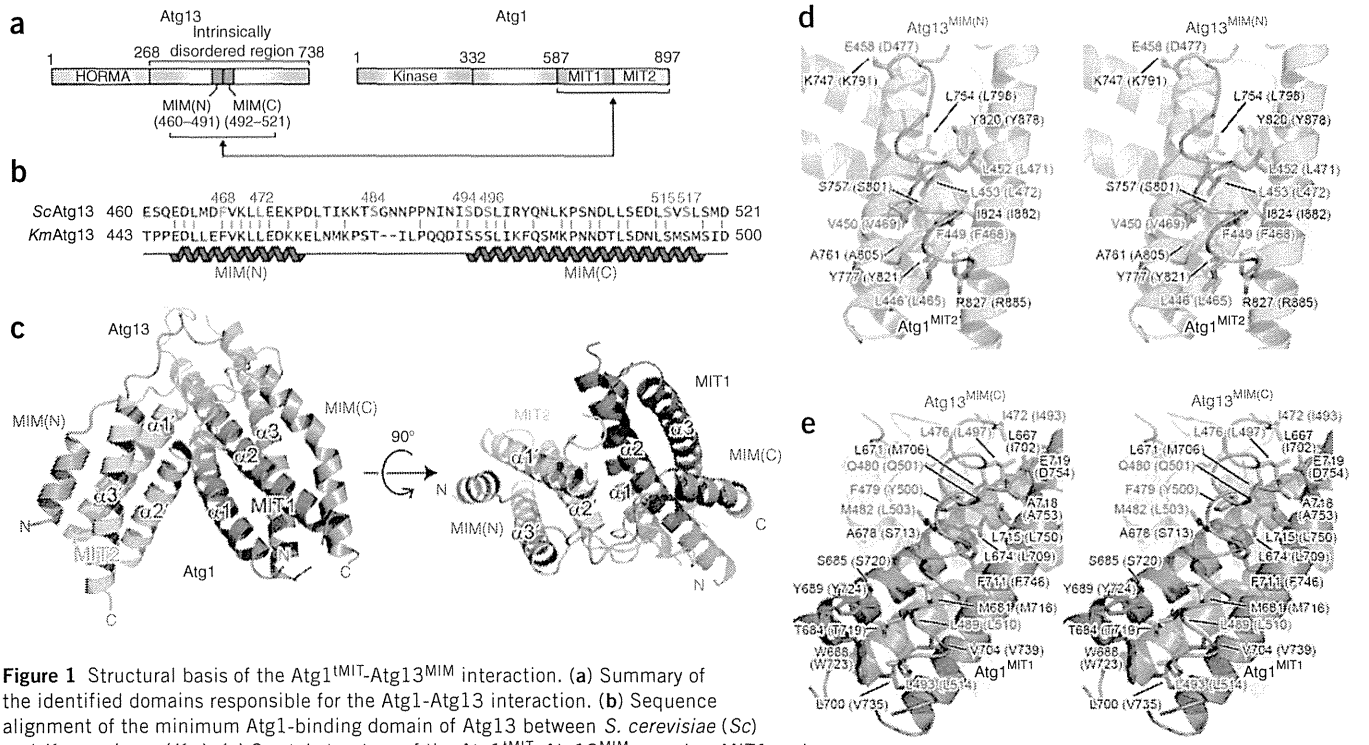

Figure 1 Structural basis of the Atg1^{tMIT}-Atg13^{MIM} interaction. (**a**) Summary of the identified domains responsible for the Atg1-Atg13 interaction. (**b**) Sequence alignment of the minimum Atg1-binding domain of Atg13 between *S. cerevisiae* (*Sc*) and *K. marxianus* (*Km*). (**c**) Crystal structure of the Atg1^{tMIT}–Atg13^{MIM} complex. MIT1 and MIT2 of Atg1 are colored blue and cyan, respectively, and Atg13^{MIM} is colored salmon pink. N and C termini are labeled N and C, respectively. All structural models in this manuscript were prepared with PyMOL (http://www.pymol.org/). (**d**,**e**) Stereo views of the interactions between Atg1^{MIT2} and Atg13$^{MIM(N)}$ (**d**) and between Atg1^{MIT1} and Atg13$^{MIM(C)}$ (**e**). Coloring is the same as in **c**. The side chains of the residues involved in the interaction are shown by a stick model in which nitrogen, oxygen and sulfur atoms are colored blue, red and yellow, respectively. The amino acids with numbers in parentheses refer to corresponding *Sc*Atg residues.

Atg13-mediated interactions is essential for revealing the architecture and the regulatory mechanism of the Atg1 complex. Atg13 comprises the N-terminal globular domain (residues 1–267), which has recently been shown to have a fold similar to HORMA domains[14], and the C-terminal region (residues 268–738), which is predicted to be intrinsically disordered (**Fig. 1a** and **Supplementary Fig. 1a**). It was previously reported that the C-terminal region of Atg13 interacts with Atg1 (refs. 7,12). We found that 62 amino acids (residues 460–521) of Atg13 are necessary and sufficient for Atg1 binding (**Supplementary Fig. 1b**). CD spectra showed that Atg13 (460–521) is intrinsically disordered in solution (**Supplementary Fig. 1c**).

Atg13-binding region of Atg1 comprises two tandem MIT domains

Atg1 consists of the N-terminal kinase domain, the middle region and the C-terminal conserved region that is responsible for Atg13 binding[15,16] (**Fig. 1a**). We cocrystallized the C-terminal region of Atg1 and the minimum Atg1-binding domain of Atg13 from *K. marxianus* and determined its structure at 2.2-Å resolution (**Fig. 1b**,**c**, **Supplementary Fig. 1d** and **Table 1**).

The C-terminal region of Atg1 responsible for Atg13 binding comprises six α-helices (α1–α3 and α1′–α3′), which fold into two antiparallel three-helix bundles resembling each other (**Fig. 1c** and **Supplementary Fig. 1e**). These two bundles interact with each other by using helices α1, α2, α1′ and α2′, which together obstruct ~1,000 Å^2 of total surface area and fold into a single domain. The asymmetric unit contains two copies of the complex, which have a similar conformation to each other, with r.m.s. differences of 1.0 Å and 0.7 Å for 169 and 41 Cα atoms of Atg1 and Atg13, respectively (**Supplementary Fig. 1f**).

Recently, the C-terminal region of Atg1 was suggested to bind membranes and sense membrane curvature[15,16]. However, structural comparison with the Dali search engine[17] showed that the three-helix bundles of Atg1 are not structurally similar to membrane-curvature sensors such as BAR domains. Thus it is difficult to speculate on Atg1's membrane-related functions, on the basis of the structure. Intriguingly, the C-terminal region of Atg1 showed high structural similarity with the microtubule interacting and transport (MIT) domains identified in proteins such as Vta1 and Vps4 involved in multivesicular body pathways[18,19]. Thus, we named the N-terminal three-helix bundle (helices α1–α3) MIT1 and the C-terminal three-helix bundle (helices α1′–α3′) MIT2. Two tandem MIT domains (named tMIT) are also observed in Vta1, in which two MIT domains interact with each other to form a single domain similar to the C-terminal region of Atg1 (**Supplementary Fig. 1g**) that recognizes the target protein Vps60 (ref. 19). In general, MIT domains are known to mediate protein-protein interactions via interaction with MIT-interacting motifs (MIMs) in target proteins[18]. Thus, we considered that the main function of Atg1^{tMIT} (superscripts are used herein to indicate domains contained by the proteins) is the recognition of its target protein, Atg13.

Structural basis of the Atg1^{tMIT}-Atg13^{MIM} interaction

The minimum Atg1-binding domain of Atg13 comprises two α-helices and a linker connecting them (**Fig. 1b**,**c**). The N-terminal helix binds to the groove formed between α1′ and α3′ of Atg1^{MIT2}, and the C-terminal helix binds to the groove formed between α2 and α3 of Atg1^{MIT1}. These two grooves are located on opposite sides of Atg1^{tMIT}, such that the two α-helices of Atg13 bind to each groove separately.

Table 1 Data collection and refinement statistics

	Native Atg1^{tMIT}–Atg13^{MIM}	SeMet Atg1^{tMIT}–Atg13^{MIM}			Atg13^{17BR}–Atg17–Atg29–Atg31
Data collection					
Space group	$P2_1$	$P2_1$			$P2_1$
Cell dimensions					
a, *b*, *c* (Å)	52.0, 96.6, 63.3	52.1, 97.2, 64.0			148.3, 64.0, 184.6
α, β, γ (°)	90.0, 93.2, 90.0	90.0, 93.3, 90.0			90.0, 109.3, 90.0
		Peak	*Inflection*	*Remote*	
Wavelength	1.0000	0.9791	0.9794	0.9640	1.0000
Resolution (Å)	50.0–2.20 (2.24–2.20)	50.0–3.20 (3.31–3.20)	50.0–3.20 (3.31–3.20)	50.0–3.20 (3.31–3.20)	50.0–3.20 (3.26–3.20)
R_{merge}	0.105 (0.936)	0.119 (0.465)	0.108 (0.486)	0.114 (0.528)	0.108 (0.876)
$I / \sigma I$	11.4 (2.3)	8.2 (5.8)	8.0 (4.2)	7.6 (3.7)	8.6 (2.1)
Completeness (%)	99.9 (100.0)	100.0 (100.0)	99.9 (100.0)	99.9 (100.0)	99.9 (100.0)
Redundancy	15.3 (15.2)	20.8 (19.8)	13.2 (12.3)	13.2 (12.3)	5.6 (5.5)
Refinement					
Resolution (Å)	45.8–2.20				44.3–3.20
No. reflections	28,695				44,114
R_{work} / R_{free}	0.209 / 0.255				0.257 / 0.293
No. atoms					
Protein	3,874				8,905
Water	26				–
B factors (Å^2)					
Protein	36.6				94.7
Water	55.1				–
r.m.s. deviations					
Bond lengths (Å)	0.011				0.009
Bond angles (°)	1.37				1.34

Values in parentheses are for highest-resolution shell. Each data set was collected from one crystal. SeMet, selenomethionine.

These interactions are reminiscent of those between the MIT domains and MIMs: in many cases, MIM assumes a helical conformation and binds to the groove formed between two α-helices of MIT[18] (for example, **Supplementary Fig. 1g**). Thus, the minimum Atg1-binding domain of Atg13 is named MIM, and its N- and C-terminal halves are named MIM(N) and MIM(C), respectively.

Atg1^{tMIT}-Atg13^{MIM} interactions are mainly hydrophobic. In the Atg1^{MIT2}-Atg13$^{MIM(N)}$ interaction, the hydrophobic side chains of Phe449 and Leu453 in Atg13$^{MIM(N)}$ bind deeply in the hydrophobic groove formed by Leu754, Ser757, Ala761, Tyr777, Tyr820, Ile824 and Arg827 in Atg1^{MIT2} (**Fig. 1d**). These interactions obstruct ~1,200 Å^2 of the total surface area. In the Atg1^{MIT1}-Atg13$^{MIM(C)}$ interaction, the hydrophobic side chains of Ile472, Leu476 and Phe479 in Atg13$^{MIM(C)}$ bind to the hydrophobic groove formed by Leu667, Leu671, Leu674, Ala678, Phe711, Leu715 and Ala718 in Atg1^{MIT1} (**Fig. 1e**). The hydrophobic side chains of Leu489 and Leu493 in Atg13$^{MIM(C)}$ bind to another hydrophobic groove formed by Met681, Thr684, Ser685, Trp688, Tyr689, Leu700 and Val704 in Atg1^{MIT1}. These interactions obstruct ~1,800 Å^2 of the total surface area. The residues involved in the Atg13^{MIM}-Atg1^{tMIT} interaction are highly conserved among Atg1 or Atg13 homologs from related species (**Supplementary Fig. 2a,b**), thus suggesting that these interactions are also conserved and that Atg13 recognition is a key function of Atg1^{tMIT}. It should be noted that the C-terminal region of Atg1, including tMIT, is evolutionarily conserved even in higher eukaryotes such as mammals[15,20] and that an ~60-residue region of human Atg13 formed a stable complex with the C-terminal region of ULK1, the mammalian counterpart of Atg1 (**Supplementary Fig. 2c,d**). These observations suggest that the Atg13^{MIM}-Atg1^{tMIT} interaction determined here is also conserved in mammals.

Role of the Atg1^{tMIT}-Atg13^{MIM} interaction in autophagy

To validate the Atg1^{tMIT}-Atg13^{MIM} interactions observed in the crystal, we performed *in vitro* binding assays, using recombinant proteins of Atg1^{tMIT} and Atg13^{MIM} truncations or mutants (**Fig. 2a–c**). Here, Atg13^{MIM} is denoted by Atg13$^{MIM(N+C)}$ in order to clearly distinguish it from Atg13$^{MIM(N)}$ and Atg13$^{MIM(C)}$. Atg13$^{MIM(N)}$ and Atg13$^{MIM(C)}$ showed strong and weak affinity to Atg1^{tMIT}, respectively, by *in vitro* pulldown assay (**Fig. 2b**). Isothermal titration calorimetry (ITC) experiments determined the dissociation constant (K_d) between Atg13$^{MIM(N)}$ and Atg1^{tMIT} to be 2.5 μM, whereas it could not detect the interaction between Atg13$^{MIM(C)}$ and Atg1^{tMIT} at the concentration used (**Fig. 2c**). These results suggested that Atg13$^{MIM(N)}$ is the main binding site for Atg1^{tMIT}. However, compared with Atg13$^{MIM(N)}$, Atg13$^{MIM(N+C)}$ showed a seven-times-lower K_d value (0.36 μM) for interaction with Atg1^{tMIT}, thus indicating that Atg13$^{MIM(C)}$ markedly enhances the affinity of Atg13$^{MIM(N)}$ for Atg1^{tMIT}. Consistently with these observations, coimmunoprecipitation experiments showed that deletion of MIM(C) markedly, and that deletion of MIM(N) completely, impaired the interaction with Atg1 *in vivo* (**Fig. 2d**). Thus we concluded that the bipartite Atg13$^{MIM(N+C)}$ region has two distinct roles in Atg1^{tMIT} recognition *in vivo*: the Atg13$^{MIM(N)}$ region functions as a basal binding site responsible for the Atg1-Atg13 interaction, and the Atg13$^{MIM(C)}$ region has a regulatory function enhancing this interaction.

Atg13$^{MIM(N)}$ binds to the hydrophobic groove in Atg1^{MIT2} by using Phe468 and Leu472 (**Fig. 1d**). Single point mutations at Phe468 and Leu472 partially, and their double mutation severely, diminished the interaction with Atg1^{tMIT} (**Fig. 2b**). These results are consistent with the truncation data showing that Atg13$^{MIM(N)}$ is the essential region for Atg1^{tMIT} binding. CD spectra showed that F468A L472A double

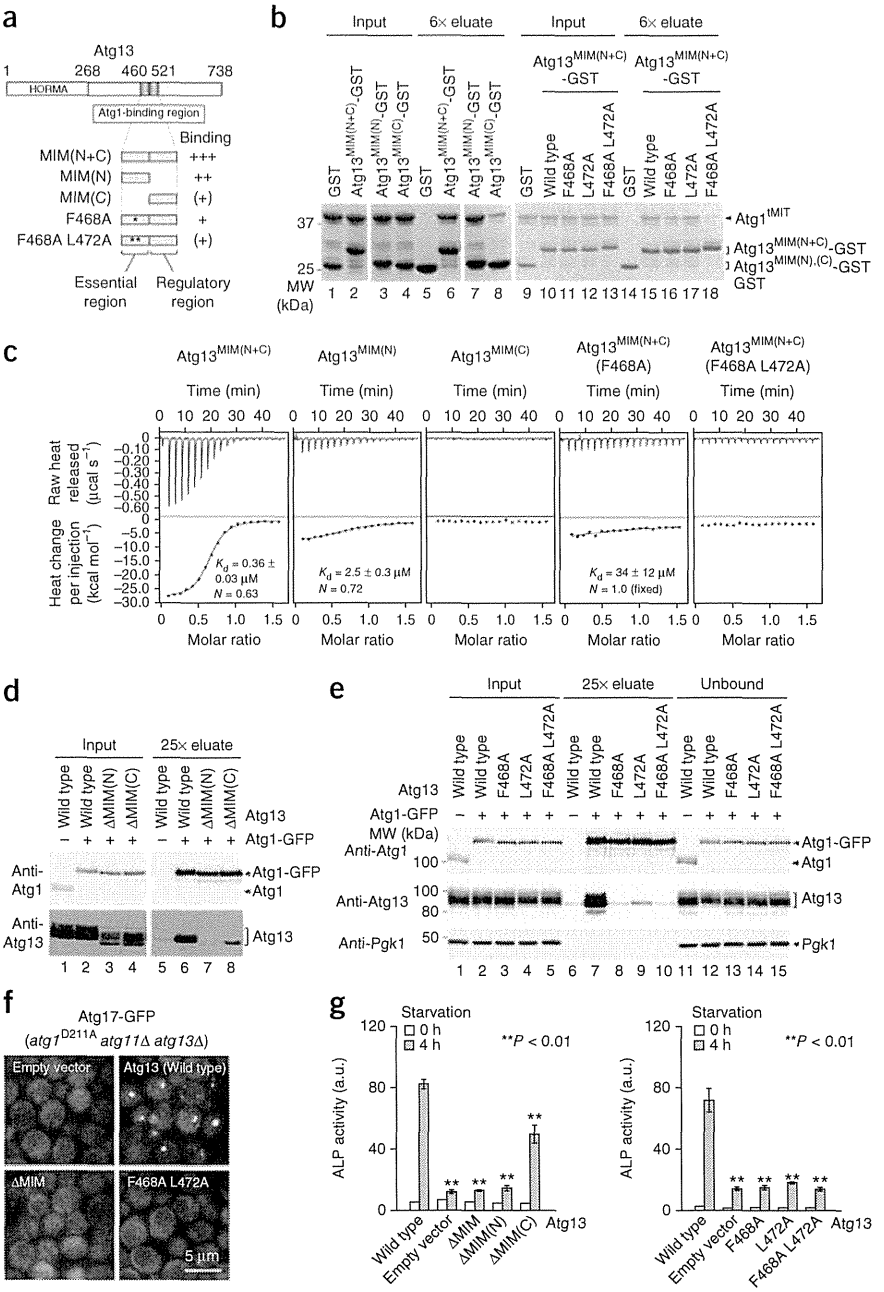

Figure 2 Molecular characterization of the Atg1^{tMIT}-Atg13^{MIM} interaction both *in vitro* and *in vivo*. (**a**) Schematic of the *in vitro* binding assays. (**b**) SDS-PAGE of *in vitro* pulldown assay between glutathione S-transferase (GST)-fused Atg13^{MIM} and Atg1^{tMIT}. MW, molecular weight. (**c**) ITC results obtained by titration of Atg13 fused to the B1 immunoglobulin domain of streptococcal protein G (GB1)[29] into a solution of Atg1^{tMIT}. *N*, stoichiometry of binding. (**d**,**e**) Western blots showing *in vivo* Atg1-Atg13 interaction analyzed by coimmunoprecipitation, for wild type and the indicated truncation (**d**) and point (**e**) mutants. Samples are yeast total lysates prepared from *ATG1-GFP* cells treated with rapamycin for 1 h (input) and immunoprecipitates isolated with anti-GFP magnetic beads (25× eluate). (**f**) Fluorescence microscopy to observe the PAS formation of Atg17-GFP in *atg13* mutant cells. Shown are *ATG17-GFP atg1*(D211A) *atg11Δ atg13Δ* cells expressing wild-type or mutant Atg13, treated with rapamycin for 2 h. (**g**) ALP assays to assess autophagic activity of *atg13* mutant cells[22]. Samples are cells grown in synthetic dextrose (SD) medium with casamino acids (SD+CA) (white bars) and cells starved in SD(−N) medium for 4 h (gray bars). A.u., arbitrary units. Error bars, s.d. (n = 3 cell cultures). $^{**}P < 0.01$ by two-tailed Student's t test. Uncropped gel images for **b**, **d** and **e** are shown in **Supplementary Figure 6a–c**.

mutation did not affect the intrinsically disordered structure of Atg13^{MIM} (**Supplementary Fig. 3a**). Alanine substitution at Phe468 and Val469 in Atg13$^{MIM(N)}$ has been reported to impair interaction with Atg1 (ref. 11), and this was also confirmed by our experiments (**Supplementary Fig. 3b**). ITC experiments revealed that, compared with wild-type Atg13^{MIM}, Atg13^{MIM}(F468A) had a K_d value 94 times higher (34 μM) for interaction with Atg1^{tMIT} and that Atg13^{MIM}(F468A L472A) did not interact with Atg1^{tMIT} at the concentration used. These data suggested that the hydrophobic interactions observed between Atg13$^{MIM(N)}$ and Atg1^{tMIT} in the crystal are actually essential for Atg1^{tMIT} binding.

Next, we studied the physiological role of the Atg1^{tMIT}-Atg13^{MIM} interaction *in vivo*. The Atg1-Atg13 interaction and its defect by F468A and L472A mutation in Atg13^{MIM} were present *in vivo* (**Fig. 2e**), irrespective of the two PAS-scaffold proteins Atg11 and Atg17 (**Supplementary Fig. 3c**). These results suggested that Phe468 and Leu472 of Atg13 are directly involved in the interaction with Atg1. We also studied the role of the Atg1^{tMIT}-Atg13^{MIM} interaction in the assembly of the PAS by monitoring Atg17-GFP under a fluorescence microscope. Atg17-GFP showed PAS localization in *atg11Δ atg13Δ* cells expressing wild-type Atg13 upon rapamycin treatment (**Fig. 2f**). In contrast, expression of Atg13$^{\Delta MIM}$ or Atg13(F468A L472A) did not restore the PAS localization of Atg17-GFP. These results clearly showed that the binding of Atg13^{MIM} to Atg1^{tMIT} is important for PAS formation under starvation conditions. In addition to triggering PAS assembly, Atg13 binding triggers the activation of Atg1 kinase upon starvation[7]. Activated Atg1 shows a slower-migrating band in SDS-PAGE, owing to autophosphorylation[21]. A slower-migrating band of Atg1 increased upon rapamycin treatment in cells expressing wild-type Atg13 but not in cells expressing Atg13(F468A L472A) (**Supplementary Fig. 3d**), thus suggesting that binding of Atg13^{MIM} to Atg1^{tMIT} is important for activating Atg1 kinase.

We also studied the role of the Atg1^{tMIT}-Atg13^{MIM} interaction in autophagy by alkaline phosphatase (ALP) assay, a method commonly used to assess autophagic activity[22]. This method uses a genetically engineered cytosolic form of ALP, Pho8Δ60, which is delivered into the vacuole by autophagy and is activated. Thus, the autophagic activity correlates well with ALP activity. Cells expressing Atg13 ΔMIM, ΔMIM(N) or point mutants at Phe468 and Leu472 in MIM(N) showed little ALP activity (**Fig. 2g**), results consistent with those obtained from binding assays (**Fig. 2b,c** and ref. 23). Intriguingly, cells expressing Atg13$^{\Delta MIM(C)}$ showed only half the activity of cells expressing wild-type Atg13. Thus both Atg1 binding by Atg13$^{MIM(N)}$

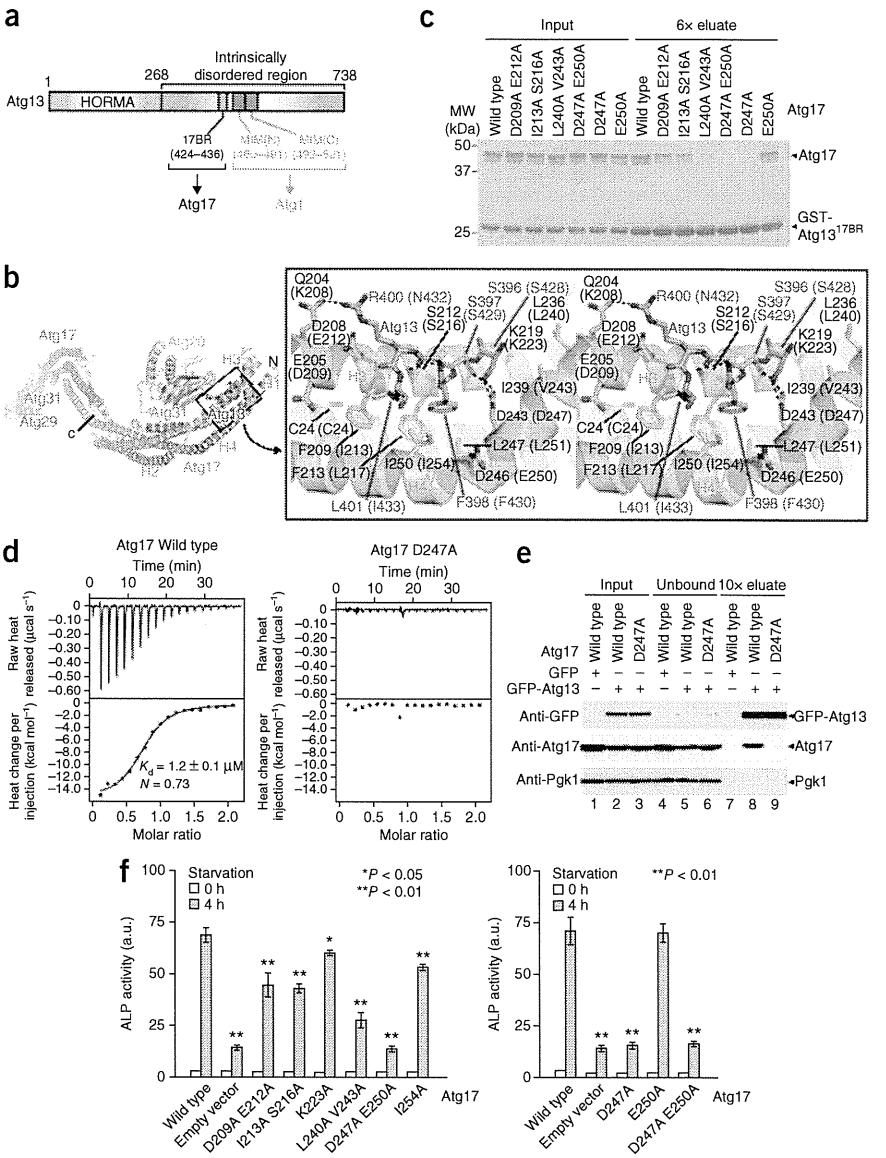

Figure 3 Structural basis of the Atg13^{17BR}-Atg17 interaction. (**a**) Summary of the Atg17-binding region of Atg13. (**b**) Crystal structure of the Atg17–Atg29–Atg31 complex cocrystallized with Atg13^{17BR}. Left, overall structure of the dimer of Atg17–Atg29–Atg31 complexes. One Atg17–Atg29–Atg31 complex is colored green (Atg17), yellow (Atg29) and orange (Atg31), whereas the other is colored gray. Atg13^{17BR} is shown as a stick model with atom coloring is as in **Figure 1d**. Right, stereo view of the Atg13-binding region. The amino acids with numbers in parentheses refer to corresponding *Sc*Atg residues. Dashed lines indicate possible hydrogen bonds between Atg13 and Atg17. (**c**) SDS-PAGE of *in vitro* pulldown assay between GST-fused Atg13^{17BR} (residues 424–436) and Atg17. (**d**) ITC results from titration of Atg13^{17BR} into a solution of Atg17. (**e**) Western blots showing *in vivo* Atg13-Atg17 interaction analyzed by coimmunoprecipitation. Samples are yeast total lysates prepared from *GFP-ATG13* cells treated with rapamycin for 1 h (input) and immunoprecipitates isolated with anti-GFP magnetic beads (10× eluate). (**f**) ALP assays to assess autophagic activity of *atg17* mutant cells. Samples are cells grown in SD+CA medium (white bars) and cells starved in SD(−N) medium for 4 h (gray bars). Error bars, s.d. (n = 3 cell cultures). $^*P < 0.05$; $^{**}P < 0.01$ by two-tailed Student's t test. Uncropped gel images for **c** and **e** are shown in **Supplementary Figure 6d,e**.

and its enhancement by Atg13$^{MIM(C)}$ are important for high autophagic activity. In yeast, aminopeptidase I (Ape1) is transported to the vacuole via the cytoplasm-to-vacuole targeting (Cvt) pathway under nutrient-rich conditions. In the vacuole, a precursor form of Ape1 is processed into a mature form that can be monitored by western blotting. We monitored the maturation of Ape1 in cells expressing the Atg13 mutant and found that F468A L472A mutation in Atg13$^{MIM(N)}$ severely impaired the Cvt pathway (**Supplementary Fig. 3d**). These results suggested that the Atg1^{tMIT}-Atg13^{MIM} interaction is essential not only for autophagy but also for the Cvt pathway.

Structural basis of the Atg13^{17BR}-Atg17 interaction

We previously reported that Atg13 interacts with Atg17 and that this interaction is essential for autophagy[7,12,13]. Therefore we studied the binding region of Atg13 for Atg17, by using recombinant proteins, and identified the minimal Atg17-binding region (17BR; residues 424–436) (**Fig. 3a** and **Supplementary Fig. 4a**). Recently, the crystal structure of the *Lachancea thermotolerans* Atg17–Atg29–Atg31 complex was reported[16]. In order to unveil the interactions between Atg13^{17BR} and Atg17 in molecular detail, we determined the crystal structure of the Atg17–Atg29–Atg31 complex cocrystallized with Atg13^{17BR}, by using *L. thermotolerans* homologs (**Table 2**). The structure of the Atg17–Atg29–Atg31 complex is essentially similar to those reported previously, consisting of two crescent-shaped Atg17 protomers interacting with each other at the C-terminal region and two Atg29–Atg31 complexes binding to the concave surface of each Atg17 protomer[16,24] (**Fig. 3b**).

The electron density map showed that Atg13^{17BR} is bound to the groove formed between the two α-helices, H3 and H4, of Atg17 (**Fig. 3b** and **Supplementary Fig. 4b**). Residues 396–401 of KtAtg13^{17BR} had defined electron density and thus were successfully modeled in one Atg17 protomer, whereas all KtAtg13^{17BR} residues could not be modeled, owing to poor electron density in another Atg17 protomer (**Supplementary Fig. 4b,c**). The Atg13-binding site of Atg17 comprises a hydrophobic pocket and its surrounding acidic residues. Phe209, Phe213, Leu247 and Ile250 of Atg17 form a hydrophobic pocket, to which the hydrophobic side chains of Phe398 and Leu401 of Atg13 are bound. In addition, Ser396 and Ser397 of Atg13 form hydrogen bonds with Atg17 Asp243.

Role of the Atg13^{17BR}-Atg17 interaction in autophagy

In order to validate the Atg13^{17BR}-Atg17 interactions observed in the crystal, we designed six Atg17 mutants for the Atg13-binding site and analyzed the binding of these mutants to Atg13 both *in vivo* and *in vitro*. An *in vitro* pulldown assay with purified recombinant proteins showed that all the mutations in Atg17 except for E250A reduced the binding to Atg13^{17BR}, among which the D247A (as well as D247A E250A) mutation was most severe (**Fig. 3c**). CD spectra showed that

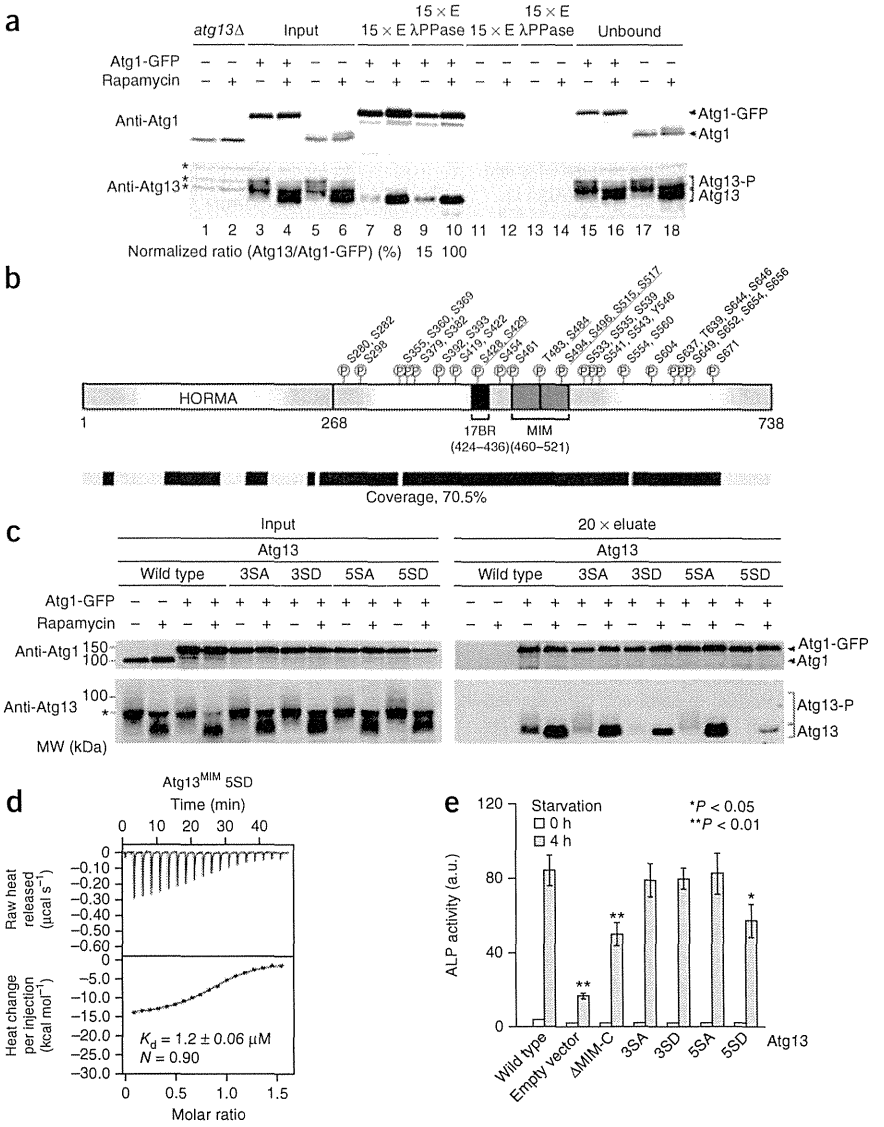

Figure 4 Phosphorylation at Atg13$^{MIM(C)}$ negatively regulates Atg1 binding. (**a**) Western blots showing the effects of rapamycin treatment on the Atg1-Atg13 interaction analyzed by coimmunoprecipitation. Samples are yeast total lysates (input) prepared from *ATG1-GFP* cells grown in nutrient-rich medium (rapamycin, –) or treated with rapamycin for 1 h (rapamycin, +) and immunoprecipitates isolated with anti-GFP magnetic beads (15× eluate (E)). λPPase indicates treatment of the immunoprecipitates with phosphatase. Intensities of the band of the coimmunoprecipitated Atg13 were measured and normalized to those of the immunoprecipitated Atg1-GFP. Asterisks, nonspecific bands; Atg13-P, phosphorylated forms of Atg13. (**b**) Summary of phosphorylation sites (P) in Atg13 dephosphorylated upon rapamycin treatment. Serine residues analyzed in this study are underlined. (**c**) Coimmunoprecipitation experiments and western blots performed as in **a**, for wild type and the indicated mutants. (**d**) ITC results from titration of Atg13(5SD) fused to GB1 into a solution of Atg1^{tMIT}. (**e**) ALP assays to assess autophagic activity of *atg13* mutant cells. Samples are cells grown in SD+CA medium (white bars) and cells starved in SD(–N) medium for 4 h (gray bars). Error bars, s.d. ($n = 3$ cell cultures). $^{**}P < 0.01$ by two-tailed Student's *t* test. Uncropped gel images for **a** and **c** are shown in **Supplementary Figure 6f,g**.

these mutations did not affect the overall structure of Atg17 (**Supplementary Fig. 4d**). *In vitro* pulldown assays also revealed that Ser428, Ser429, Phe430 and Ile433 in Atg13^{17BR}, residues directly involved in Atg17 binding, are essential for Atg17 binding (**Supplementary Fig. 4e**). It should be noted that Arg434 and Arg435 in Atg13^{17BR} and Asp209, Glu212, Leu240 and Val243 in Atg17, all of which are located near the binding site but are not directly involved in the interaction, are also important for Atg13^{17BR} binding (**Fig. 3c** and **Supplementary Fig. 4e**). Their interactions may also contribute to the affinity between Atg13^{17BR} and Atg17. We also studied the Atg13^{17BR}-Atg17 interaction quantitatively with ITC, which showed that the K_d value between Atg13^{17BR} and Atg17 is 1.2 μM, whereas Atg13^{17BR} did not show detectable binding to Atg17(D247A) and Atg17(D247A E250A) (**Fig. 3d** and **Supplementary Fig. 4f**). Coimmunoprecipitation experiments also showed that the D247A mutation in Atg17 severely reduced interaction with GFP-Atg13 *in vivo* (**Fig. 3e**). We then studied the role of the Atg13^{17BR}-Atg17 interaction in autophagy by the ALP assay, using cells expressing these mutants. All mutations except for E250A reduced the ALP activity, and the D247A mutation (as well as D247A E250A) most severely impaired activity (**Fig. 3f**). These results clearly demonstrated that the Atg13^{17BR}-Atg17 interaction observed in the crystal is actually important for Atg13-Atg17 interaction *in vivo* and for autophagy progression.

Phosphorylation of Atg13$^{MIM(C)}$ regulates Atg1 binding

The structural basis of the interactions of Atg13 with Atg1 and Atg17 has been established. The next question is how these interactions are regulated. The Atg1-Atg13 interaction has been previously reported to be regulated by nutrient conditions[7]; however, a recent study showed that Atg1 and Atg13 constitutively form a complex irrespective of nutrient conditions[11]. In order to resolve this discrepancy, we reexamined whether nutrient conditions regulate the Atg1-Atg13 interaction. Because Atg13 is easily dephosphorylated by resident phosphatases during the preparation of cell lysates, we carefully prepared cell lysates by cooling and adding sufficient amounts of various phosphatase inhibitors (Online Methods). Under nutrient-rich conditions, Atg13 was hyperphosphorylated and showed a smear and slower-migrating band, which was dephosphorylated and shifted into a faster and less smeared band upon rapamycin treatment (**Fig. 4a**). The amount of Atg13 coimmunoprecipitated with Atg1-GFP increased substantially upon rapamycin treatment (**Fig. 4a**). To quantify the amount of coimmunoprecipitated Atg13, we added λ protein phosphatase (λPPase) to the eluates after immunoprecipitation and quantified the sharp band of the dephosphorylated Atg13. Our results showed that the ratio of coimmunoprecipitated Atg13 from rapamycin-treated and growing cells was about 7:1 (**Fig. 4a**). The enhancement of the Atg1-Atg13 interaction by rapamycin treatment was also present when we used the same buffer conditions with the coimmunoprecipitation

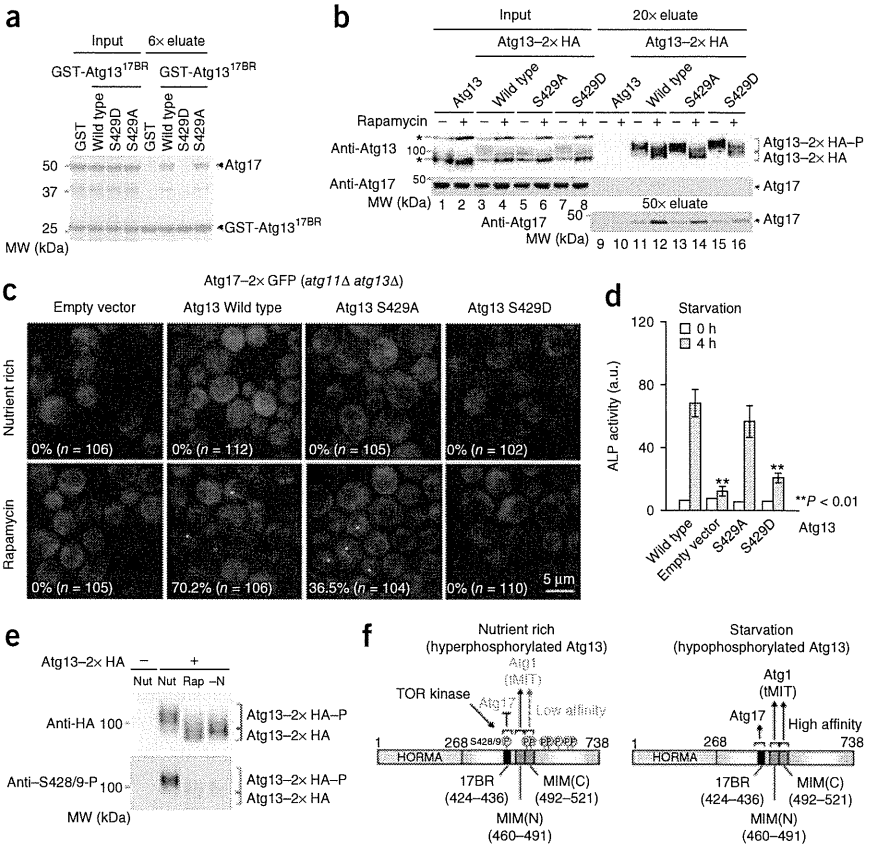

Figure 5 Dephosphorylation of Ser429 in Atg13 is required for Atg17 binding, PAS assembly and autophagy. (**a**) SDS-PAGE of *in vitro* pulldown assay between GST-fused Atg13^{17BR} and Atg17. (**b**) Coimmunoprecipitation experiments to assess Atg13-Atg17 interaction *in vivo*. Samples are yeast total lysates (input) prepared from *ATG13–2× HA* cells grown in nutrient-rich medium (rapamycin, –) or treated with rapamycin for 1 h (rapamycin, +) with immunoprecipitates isolated with anti-HA beads (20× eluate). Asterisks indicate nonspecific bands. Atg13–2× HA–P indicates phosphorylated forms of Atg13–2× HA. (**c**) Fluorescence microscopy to observe the PAS formation of Atg17–2× GFP in *atg13* mutant cells. Shown are *ATG17–2× GFP atg11Δ atg13Δ* cells expressing wild-type or mutant Atg13, grown in nutrient-rich medium (top) and those treated with rapamycin for 2 h (bottom). (**d**) ALP assays to assess autophagic activity of *atg13* mutant cells. Samples are cells grown in SD+CA medium (white bars) and cells starved in SD(–N) medium for 4 h (gray bars). Error bars, s.d. ($n = 3$ cell cultures). $^{**}P < 0.01$ by two-tailed Student's *t* test. (**e**) Western blots showing the phosphorylation state of Atg13–2× HA, probed with anti-HA antibodies or antibodies specific to phosphorylated Ser428 or Ser429 as indicated. Samples are immunoprecipitates of anti-HA immunoprecipitation prepared from cells grown in nutrient-rich medium (Nut), treated with rapamycin for 1 h (Rap) or starved for 1 h (–N). (**f**) Summary of starvation-induced interactions of Atg13 with Atg1 and Atg17. Uncropped gel images for **a**, **b** and **e** are shown in **Supplementary Figure 6h–j**.

experiments reported by Kraft *et al.*[11] (**Supplementary Fig. 5a**). To further confirm that the Atg1-Atg13 interaction is enhanced upon rapamycin treatment, we also performed coimmunoprecipitation experiments on cells expressing Atg13 with a tandem hemagglutinin tag (2× HA) and western blotting with anti-HA antibody. These results also showed that the coimmunoprecipitated Atg13–2× HA from rapamycin-treated cells was markedly higher than that from growing cells (**Supplementary Fig. 5b**). Thus, we concluded that starvation induces dephosphorylation of Atg13 and that this consequently enhances the affinity of Atg13 to Atg1, as we reported previously.

So how, then, does the phosphorylation state of Atg13 regulate its interaction with Atg1? Dozens of phosphorylation sites of Atg13 have been reported by several groups including ours[6,25,26]. Here we reexamined the phosphorylation sites of Atg13 by LC-MS/MS analysis of the samples prepared from yeast cells overexpressing GFP-Atg13 with and without rapamycin. We identified 51 phosphorylated sites whose phosphorylation level was reduced upon rapamycin treatment (**Fig. 4b** and **Supplementary Tables 1** and **2**), including six sites located in the structure of Atg13^{MIM}: Thr483 and Ser484 at the linker between the MIM(N) and MIM(C) helices and Ser494, Ser496, Ser515 and Ser517 at the MIM(C) helix. We prepared two phosphorylation-mimic mutants, 3SD (aspartate substitution at Ser484, Ser494 and Ser496) and 5SD (aspartate substitution at Ser484, Ser494, Ser496, Ser515 and Ser517), and their corresponding alanine mutants, 3SA and 5SA. Coimmunoprecipitation experiments showed that 3SD mutation partially, and 5SD mutation markedly, impaired the interaction with Atg1, whereas 3SA and 5SA did not impair the interaction at all (**Fig. 4c**). We then studied the interaction between the Atg13^{MIM} 5SD mutant and Atg1^{tMIT} *in vitro* with ITC, which showed that the K_d value for Atg13^{MIM} 5SD and Atg1^{tMIT} is 1.2 μM (**Fig. 4d**), three times higher than that of wild-type Atg13^{MIM} and Atg1^{tMIT} (**Fig. 2c**). These data suggested that phosphorylation at MIM(C) impairs this domain's enhancing role in the affinity of MIM(N) for Atg1^{tMIT} and subsequently leads to the marked decrease in abundance of the Atg1–Atg13 complex *in vivo*. ALP assays showed that the 5SD mutation partially impaired autophagic activity, so that it was almost comparable to the activity observed for ΔMIM(C) (**Fig. 4e**). Together, these data suggested that the phosphorylation at five serines in Atg13$^{MIM(C)}$ weakens the affinity of Atg13 with Atg1 and thus results in the decreased population of the Atg1 complex and the partial repression of autophagy.

Dephosphorylation of Atg13^{17BR} induces Atg17 binding

The Atg13-Atg17 interaction, in addition to the Atg1-Atg13 interaction, is also upregulated upon starvation[13], thus suggesting that it is also regulated by Atg13 phosphorylation. Atg13^{17BR} contains four serine residues, of which Ser428 and Ser429 were included in 51 phosphorylation sites (**Fig. 4b**). Both Ser428 and Ser429 make hydrogen bonds with Asp247 in Atg17 (**Fig. 3b**), and this bonding is essential for the Atg13^{17BR}-Atg17 interaction (**Supplementary Fig. 4e**). Phosphorylation of these serines would not only block the formation of these important hydrogen bonds but also cause electrostatic repulsion between negatively charged phosphate groups and Asp247. In fact, the phosphorylation-mimic aspartate substitution of Ser429 severely diminished the Atg13^{17BR}-Atg17 interaction, although its alanine substitution impaired it only partially *in vitro* (**Fig. 5a**). These results suggest that the Atg13^{17BR}-Atg17 interaction is negatively regulated by the phosphorylation of these serines in Atg13^{17BR}.

In order to further characterize the role of Ser429 phosphorylation *in vivo*, we next performed coimmunoprecipitation experiments with Ser429 mutants of Atg13. Rapamycin treatment prominently

increased the amount of Atg17 coimmunoprecipitated with wild-type Atg13–2× HA (**Fig. 5b**). This observation is consistent with a previous report showing that Atg13 interacted with Atg17 in a starvation-dependent manner[13]. Atg13(S429D)–2× HA showed a severe defect in Atg17 binding, whereas Atg13(S429A)–2× HA retained moderate affinity with Atg17 (**Fig. 5b**). We subjected the same panel of Atg13 mutants to coimmunoprecipitation experiments with Atg1, and these showed that neither the S429A nor the S429D mutation affected the interaction with Atg1 (**Supplementary Fig. 5c**). These results suggested that the S429D mutation specifically diminishes the interaction with Atg17 *in vivo*.

Next, we studied the PAS localization of Atg17–2× GFP in *atg11Δ atg13Δ* cells expressing the same panel of Atg13 mutants. In cells expressing wild-type Atg13 or Atg13(S429A), Atg17–2× GFP appeared as a bright dot, whereas no dots were present in cells expressing Atg13(S429D) or containing an empty vector (**Fig. 5c**). Phosphorylation at Ser429 should block the PAS assembly by specifically impairing the Atg13-Atg17 interaction. Finally, we studied the autophagic activity of cells expressing Atg13 mutants by using the ALP assay (**Fig. 5d**). The S429D mutation severely impaired the autophagic activity, whereas S429A mutation impaired it only partially. These data suggested that dephosphorylation at Ser429 in Atg13 promotes PAS assembly and autophagy progression by enhancing the interaction with Atg17.

To further confirm the starvation-dependent dephosphorylation of Ser428 and Ser429 in Atg13 *in vivo*, we generated antibodies to Atg13(425–436) with a phosphate group at both Ser428 and Ser429 (named anti–Ser428/9-P) by using synthesized phosphopeptides as antigens (**Supplementary Fig. 5d,e**). Under nutrient-rich conditions, the Atg13 bands were clearly detected by anti–Ser428/9-P antibody, whereas they were severely diminished upon starvation or rapamycin treatment (**Fig. 5e**). These results clearly demonstrated that Ser428 and Ser429 of Atg13 are phosphorylated under nutrient-rich conditions and dephosphorylated under autophagy-inducing conditions. Taken together, our results led us to the conclusion that starvation triggers the dephosphorylation of Ser428 and Ser429 in Atg13, and this in turn markedly increases the affinity of $Atg13^{17BR}$ for Atg17 and promotes the formation of the Atg1 complex, thereby leading to the PAS assembly and autophagy initiation.

DISCUSSION

Here we performed crystallographic studies on $Atg1^{tMIT}$–$Atg13^{MIM}$ and $Atg13^{17BR}$–Atg17 complexes and unveiled the molecular interactions essential for the construction of the Atg1 complex, the core of the PAS responsible for starvation-induced autophagy. We proposed a model of starvation-induced formation of the Atg1 complex, on the basis of the structural data and the findings of mutational analyses, both *in vitro* and *in vivo* (**Fig. 5f**).

Under nutrient-rich conditions, Atg13 is hyperphosphorylated by TORC1 (ref. 6), and this attenuates the interaction of Atg13 with both Atg1 and Atg17. The $Atg13^{17BR}$-Atg17 interaction, which is mediated by the hydrophobic and hydrophilic interactions between $Atg13^{17BR}$ and the acidic Atg13-binding site of Atg17, is directly impaired by the phosphate group introduced at Ser429 in $Atg13^{17BR}$, owing to electrostatic repulsion. Phosphorylation of Ser428 would also weaken the interaction by a similar mechanism. However, the Atg1-Atg13 interaction, which uses MIT-MIM interactions generally used for protein-protein interactions, is regulated by phosphorylation of the serines in $Atg13^{MIM(C)}$ but not in $Atg13^{MIM(N)}$, the most important region for Atg1 binding (**Figs. 2a–c** and **4c,d**). $Atg13^{MIM(C)}$ may function as a regulator for the formation of the Atg1–Atg13 complex *in vivo*. It should be noted that 5SA mutation did not enhance the Atg1-Atg13 interaction under nutrient-rich conditions, thus suggesting that additional phosphorylation sites may be required for regulating the Atg1-Atg13 interaction more strictly. We previously proposed an autophagy-initiation model: dephosphorylation of Atg13 enhances its interaction with Atg1, which in turn triggers autophagy. Here, we obtained new insights that dephosphorylation of Atg13 also enhances Atg13's interaction with Atg17. Thus we update the autophagy-initiation model as follows: upon starvation, dephosphorylated Atg13 binds to both Atg1 and Atg17, and this promotes formation of the Atg1 complex, PAS assembly and autophagy progression. Phosphoregulation of two distinct interactions (Atg13-Atg1 and Atg13-Atg17) would be more favorable for rigorous, accurate regulation of autophagy.

ULK1 forms a complex with mammalian Atg13 and with FIP200, a functional counterpart of yeast Atg17, and it exerts an essential role in the initiation of mammalian autophagy, similarly to the Atg1 complex in yeast[27]. The MIT-MIM interaction observed in the Atg1–Atg13 complex also appears to be used in the mammalian ULK1–Atg13 complex (**Supplementary Fig. 2c,d**). Most serines in $Atg13^{MIM}$ are not conserved in mammalian Atg13 (**Supplementary Fig. 2c**); this is consistent with previous reports that ULK1 constitutively forms a complex with Atg13 irrespective of nutrient conditions. In the case of the mammalian Atg13-FIP200 interaction, it is difficult to speculate on its binding mode on the basis of the $Atg13^{17BR}$-Atg17 interaction, because FIP200 has little sequence homology with Atg17. However, considering that FIP200 is predicted to possess coiled coils, similarly to Atg17 (ref. 28), it might be possible that Atg13 binds FIP200 in a manner similar to that in Atg17 binding. Structural comparison between the ULK1 and Atg1 complexes will clarify their similarities and differences in molecular detail and will contribute to the establishment of the common basic mechanisms underlying autophagy initiation.

METHODS

Methods and any associated references are available in the online version of the paper.

Accession codes. The structures of the $Atg1^{tMIT}$–$Atg13^{MIM}$ and $Atg13^{17BR}$–Atg17–Atg29–Atg31 complexes have been deposited in the Protein Data Bank under accession codes 4P1N and 4P1W, respectively.

Note: Any Supplementary Information and Source Data files are available in the online version of the paper.

ACKNOWLEDGMENTS

The synchrotron radiation experiments were performed at beamlines BL41XU at SPring8 and NW12A at Photon Factory, Japan. This work was supported in part by Japan Society for the Promotion of Sciences KAKENHI, grant nos. 24113725 and 25111004 (to N.N.N.), 2440279 (to Y.F.), 30114416 (to Y.O.) and 24770182 (to H.Y.), and by the Targeted Proteins Research Program from the Ministry of Education, Culture, Sports, Science and Technology of Japan (to Y.O. and F.I.).

AUTHOR CONTRIBUTIONS

Y.F. and N.N.N. performed structural studies; Y.F. performed biochemical studies; S.W.S., H.Y. and C.K.-K. performed yeast experiments; R.A. cloned the Atg homolog from *K. marxianus*; Y.K. and H.H. performed LC-MS/MS analysis; and Y.F., S.W.S., H.Y., F.I., Y.O. and N.N.N. analyzed data and wrote the manuscript. All authors discussed the results and commented on the manuscript. N.N.N. and Y.O. supervised the work.

COMPETING FINANCIAL INTERESTS

The authors declare no competing financial interests.

1. Mizushima, N. & Komatsu, M. Autophagy: renovation of cells and tissues. *Cell* **147**, 728–741 (2011).
2. Mizushima, N., Yoshimori, T. & Ohsumi, Y. The role of Atg proteins in autophagosome formation. *Annu. Rev. Cell Dev. Biol.* **27**, 107–132 (2011).
3. Suzuki, K. & Ohsumi, Y. Current knowledge of the pre-autophagosomal structure (PAS). *FEBS Lett.* **584**, 1280–1286 (2010).
4. Suzuki, K. *et al.* The pre-autophagosomal structure organized by concerted functions of APG genes is essential for autophagosome formation. *EMBO J.* **20**, 5971–5981 (2001).
5. Noda, T. & Ohsumi, Y. Tor, a phosphatidylinositol kinase homologue, controls autophagy in yeast. *J. Biol. Chem.* **273**, 3963–3966 (1998).
6. Kamada, Y. *et al.* Tor directly controls the Atg1 kinase complex to regulate autophagy. *Mol. Cell. Biol.* **30**, 1049–1058 (2010).
7. Kamada, Y. *et al.* Tor-mediated induction of autophagy via an Apg1 protein kinase complex. *J. Cell Biol.* **150**, 1507–1513 (2000).
8. Kabeya, Y. *et al.* Characterization of the Atg17-Atg29-Atg31 complex specifically required for starvation-induced autophagy in *Saccharomyces cerevisiae*. *Biochem. Biophys. Res. Commun.* **389**, 612–615 (2009).
9. Kawamata, T., Kamada, Y., Kabeya, Y., Sekito, T. & Ohsumi, Y. Organization of the pre-autophagosomal structure responsible for autophagosome formation. *Mol. Biol. Cell* **19**, 2039–2050 (2008).
10. Cheong, H., Nair, U., Geng, J. & Klionsky, D.J. The Atg1 kinase complex is involved in the regulation of protein recruitment to initiate sequestering vesicle formation for nonspecific autophagy in *Saccharomyces cerevisiae*. *Mol. Biol. Cell* **19**, 668–681 (2008).
11. Kraft, C. *et al.* Binding of the Atg1/ULK1 kinase to the ubiquitin-like protein Atg8 regulates autophagy. *EMBO J.* **31**, 3691–3703 (2012).
12. Cheong, H. *et al.* Atg17 regulates the magnitude of the autophagic response. *Mol. Biol. Cell* **16**, 3438–3453 (2005).
13. Kabeya, Y. *et al.* Atg17 functions in cooperation with Atg1 and Atg13 in yeast autophagy. *Mol. Biol. Cell* **16**, 2544–2553 (2005).
14. Jao, C.C., Ragusa, M.J., Stanley, R.E. & Hurley, J.H.A. HORMA domain in Atg13 mediates PI 3-kinase recruitment in autophagy. *Proc. Natl. Acad. Sci. USA* **110**, 5486–5491 (2013).
15. Chan, E.Y., Longatti, A., McKnight, N.C. & Tooze, S.A. Kinase-inactivated ULK proteins inhibit autophagy via their conserved C-terminal domains using an Atg13-independent mechanism. *Mol. Cell. Biol.* **29**, 157–171 (2009).
16. Ragusa, M.J., Stanley, R.E. & Hurley, J.H. Architecture of the Atg17 complex as a scaffold for autophagosome biogenesis. *Cell* **151**, 1501–1512 (2012).
17. Holm, L., Kaariainen, S., Rosenstrom, P. & Schenkel, A. Searching protein structure databases with DaliLite v.3. *Bioinformatics* **24**, 2780–2781 (2008).
18. Hurley, J.H. & Yang, D. MIT domainia. *Dev. Cell* **14**, 6–8 (2008).
19. Xiao, J. *et al.* Structural basis of Vta1 function in the multivesicular body sorting pathway. *Dev. Cell* **14**, 37–49 (2008).
20. Matsuura, A., Tsukada, M., Wada, Y. & Ohsumi, Y. Apg1p, a novel protein kinase required for the autophagic process in *Saccharomyces cerevisiae*. *Gene* **192**, 245–250 (1997).
21. Yeh, Y.Y., Wrasman, K. & Herman, P.K. Autophosphorylation within the Atg1 activation loop is required for both kinase activity and the induction of autophagy in *Saccharomyces cerevisiae*. *Genetics* **185**, 871–882 (2010).
22. Noda, T., Matsuura, A., Wada, Y. & Ohsumi, Y. Novel system for monitoring autophagy in the yeast *Saccharomyces cerevisiae*. *Biochem. Biophys. Res. Commun.* **210**, 126–132 (1995).
23. Lynch-Day, M.A. & Klionsky, D.J. The Cvt pathway as a model for selective autophagy. *FEBS Lett.* **584**, 1359–1366 (2010).
24. Mao, K. *et al.* Atg29 phosphorylation regulates coordination of the Atg17-Atg31-Atg29 complex with the Atg11 scaffold during autophagy initiation. *Proc. Natl. Acad. Sci. USA* **110**, E2875–E2884 (2013).
25. Stephan, J.S., Yeh, Y.Y., Ramachandran, V., Deminoff, S.J. & Herman, P.K. The Tor and PKA signaling pathways independently target the Atg1/Atg13 protein kinase complex to control autophagy. *Proc. Natl. Acad. Sci. USA* **106**, 17049–17054 (2009).
26. Soulard, A. *et al.* The rapamycin-sensitive phosphoproteome reveals that TOR controls protein kinase A toward some but not all substrates. *Mol. Biol. Cell* **21**, 3475–3486 (2010).
27. Mizushima, N. The role of the Atg1/ULK1 complex in autophagy regulation. *Curr. Opin. Cell Biol.* **22**, 132–139 (2010).
28. Hara, T. *et al.* FIP200, a ULK-interacting protein, is required for autophagosome formation in mammalian cells. *J. Cell Biol.* **181**, 497–510 (2008).
29. Kobashigawa, Y., Kumeta, H., Ogura, K. & Inagaki, F. Attachment of an NMR-invisible solubility enhancement tag using a sortase-mediated protein ligation method. *J. Biomol. NMR* **43**, 145–150 (2009).

ONLINE METHODS

Plasmid construction of *Escherichia coli* expression vectors. To construct coexpression plasmids encoding *Km*Atg1(566–836) and *Km*Atg13(441–500), the genes were amplified by PCR and cloned into pGEX-6P-1 (GE Healthcare) and pACYC184 with the T7 promoter, respectively. To construct coexpression plasmids encoding full-length *Lt*Atg17, *Lt*Atg29(1–86) and hexahistidine (His_6)-tagged full-length *Lt*Atg31, the genes were amplified by PCR and cloned into pACYC184 with the T7 promoter for *Lt*Atg17 and pRSFDuet-1 vector (Novagen) for *Lt*Atg29(1–86) and His_6-tagged *Lt*Atg31. To construct coexpression plasmids encoding *Sc*Atg31(174–196) and *Sc*Atg17, the genes were amplified by PCR and cloned into pGEX-6P-1 and pET28a(+) vector (Novagen), respectively. To construct expression plasmids encoding *Sc*Atg1(587–897), various lengths of *Sc*Atg13, and full-length *Sc*Atg17, the genes were amplified by PCR and cloned into pGEX-6P-1 (*Sc*Atg1 and *Sc*Atg13), into a modified version of pET-11a (Novagen) into which His_6 and the GST genes had already been inserted (*Sc*Atg13), and into pCold-TF (Takara Bio) (Atg17). To construct expression plasmids encoding various lengths of *Sc*Atg13-GB1-His_6, the *ScATG13* gene was amplified by PCR and cloned into a modified version of pGEX-6P-1 into which the GB1 and His_6 genes had already been inserted. Mutations leading to the indicated amino acid substitutions were introduced by PCR-mediated site-directed mutagenesis. All of the constructs were sequenced to confirm their identities.

Plasmid construction of yeast expression vectors. The low-copy plasmid for expression of Atg13 under control of the *ATG13* own promoter was constructed as follows: a DNA fragment including the *ATG13* promoter, the *ATG13* gene, and the *ATG13* terminator (from a 1,000-bp upstream region of the initiation codon to a 250-bp downstream region of the termination codon of the *ATG13* gene) was amplified from yeast genomic DNA, digested with SalI and XhoI, and inserted into the SalI-XhoI site of pRS316 (ref. 30), to yield pRS316-ATG13. The low-copy plasmid for expression of Atg13–2× HA under control of the *ATG13* own promoter was constructed as follows: a DNA fragment encoding the 2× HA sequence was inserted into pRS316-ATG13 just upstream of the stop codon of the *ATG13* gene by PCR-mediated site-directed mutagenesis, to yield pRS316–ATG13–2× HA. The low-copy plasmid for expression of Atg17 under control of the *ATG17* own promoter was constructed as follows: a DNA fragment including the *ATG17* promoter, the *ATG17* gene, and the *ATG17* terminator (from a 2,000-bp upstream region of the initiation codon to a 250-bp downstream region of the termination codon of the *ATG17* gene) was amplified from yeast genomic DNA, digested with SalI and BamHI, and inserted into the SalI-BamHI site of pRS316 (ref. 30), to yield pRS316-ATG17. The low-copy plasmid for expression of GFP-Atg13 under control of the *ADH1* promoter was constructed as follows: DNA fragments including the *ADH1* promoter, the *GFP* gene, or *PGK1* terminator were amplified, digested with XhoI and XbaI and inserted into the XhoI-XbaI site of pRS314 (ref. 30), to yield pRS314-ADHpro-GFP-PGKterm. A DNA fragment including the *ATG13* gene was amplified, digested with BamHI, and inserted into the BamHI site of pRS314-ADHpro-GFP-PGKterm, to yield pRS314-ADHpro-GFP-Atg13-PGKterm. All of the constructs were sequenced to confirm their identities.

Protein expression and purification. *E. coli* strain BL21 (DE3) cells were used for expression of all recombinant proteins. For crystallization of the $Atg1^{tMIT}$–$Atg13^{MIM}$ complex, *Km*Atg13(441–500) was coexpressed with GST-*Km*Atg1(566–836). After cell lysis, *Km*Atg1 (566–836) was purified by affinity chromatography on a glutathione–Sepharose 4B (GS4B) column (GE Healthcare). After affinity chromatography, GST was excised from *Km*Atg1(566–836) with human rhinovirus 3C protease. The protein complex was again applied to a GS4B column after exchange of the solvent with phosphate-buffered saline (PBS). Finally, it was purified on a HiLoad 26/60 Superdex 200 PG column (GE Healthcare) eluted with 20 mM Tris-HCl, pH 8.0 and 150 mM NaCl. For crystallization of the $Atg13^{17BR}$–Atg17–Atg29–Atg31 complex, His_6-tagged *Lt*Atg31 was coexpressed with *Lt*Atg17 and *Lt*Atg29(1–86). After cell lysis, *Lt*Atg31 was purified by affinity chromatography with a Ni-NTA column (Qiagen). After affinity chromatography, the protein complex was purified on a HiLoad 26/60 Superdex 200 PG column eluted with 20 mM Tris-HCl, pH 8.0 and 150 mM NaCl. For *in vitro* pulldown assays, various lengths of GST-*Sc*Atg13 and His_6–*Sc*Atg13-GST, GST-*Sc*Atg1(587–897) and GST-*Sc*Atg31(174–196)-*Sc*Atg17 complex were first purified with a GS4B column. After affinity chromatography, GST was excised from GST-*Sc*Atg1(587–897) and GST-*Sc*Atg31(174–196)–*Sc*Atg17 complex with human rhinovirus 3C protease. *Sc*Atg1(587–897) and *Sc*Atg31(174–196)–*Sc*Atg17 complex were again applied to a GS4B column in order to remove the excised GST. Various lengths of His_6-ScAtg13-GST were then purified by affinity chromatography with a Ni-NTA column. His_6-tagged trigger factor fused to *Sc*Atg17 (His_6-TF-*Sc*Atg17) was first applied to a Ni-NTA column, and this was followed by on-column digestion with human rhinovirus 3C protease. *Sc*Atg17 digested and released from the column was then applied to a GS4B column to remove the protease. Purified proteins were buffer-exchanged with PBS before *in vitro* pulldown assay. For ITC analyses and CD spectroscopy (described in **Supplementary Note**), GST-ScAtg13^{MIM}-GB1-His_6 was first purified with a GS4B column. After affinity chromatography, GST was excised from the proteins with human rhinovirus 3C protease. Next, the proteins were purified with a Ni-NTA column. Finally, the protein was purified on a HiLoad 26/60 Superdex 200 PG column eluted with PBS. *Sc*Atg1(587–897) and *Sc*Atg31(174–196)–*Sc*Atg17 complex were first purified as described above and then were purified on a HiLoad 26/60 Superdex 200 PG column eluted with PBS. ScAtg13^{17BR} peptide (residues 424–436; purchased from Operon) was purified on a Superdex Peptide 10/300 GL column eluted with PBS.

Crystallization. All crystallization trials were performed with the sitting-drop vapor-diffusion method at 20 °C. For crystallization of the *K. marxianus* $Atg1^{tMIT}$–$Atg13^{MIM}$ complex, drops (0.3 µl) of 15 mg ml^{-1} *Km*ATG1(566–836)–*Km*ATG13(441–500) in 20 mM Tris buffer, pH 8.0 and 150 mM NaCl were mixed with reservoir solution consisting of 0.2 M ammonium acetate, 12% polyethylene glycol 3350 and 0.1 M acetate buffer, pH 4.8, and equilibrated against 100 µl of the same reservoir solution by vapor diffusion. For crystallization of the *L. thermotolerans* Atg13–Atg17–Atg29–Atg31 complex, drops (0.3 µl) of 2 mg ml^{-1} *Lt*Atg17–*Lt*Atg29(1–87)–*Lt*Atg31 with 1 mM LtAtg13^{17BR} peptide (residues 392–404; purchased from Operon) in 20 mM Tris buffer, pH 8.0, and 150 mM NaCl were mixed with equal amounts of reservoir solution consisting of 8% polyethylene glycol monomethyl ether 5000, 100 mM Tris buffer, pH 8.5 and equilibrated against 100 µl of the same reservoir solution by vapor diffusion.

X-ray crystallography. Diffraction data were collected with a Rayonix MX-225 CCD detector at a SPring-8 beamline BL41XU for the $Atg1^{tMIT}$–$Atg13^{MIM}$ complex and with an ADSC Quantum 210 CCD detector at a Photon Factory beamline NW12A for the $Atg13^{17BR}$–Atg17–Atg29–Atg31 complex. All diffraction data were processed with HKL2000 (ref. 31). The initial phasing of the $Atg1^{tMIT}$–$Atg13^{MIM}$ complex was performed by the multiwavelength anomalous dispersion method with the peak, inflection and high-remote data of the selenomethionine-labeled crystal. After 23 selenium sites were identified and the initial phases calculated, density modification and automated model building were performed with Phenix[32]. The structure of the $Atg13^{17BR}$–Atg17–Atg29–Atg31 complex was determined by the molecular replacement method with MOLREP[33] in CCP4 (ref. 34), for which the Atg17–Atg29–Atg31 complex structure (PDB 4HPQ) was used as a search model. For both complex structures, further model building was performed manually with Coot[35], and crystallographic refinement with noncrystallographic symmetry restrains was performed with CNS[36] and REFMAC5 (ref. 37) in CCP4 (ref. 34).

***In vitro* pulldown assay.** Purified proteins were incubated with GST-accept beads (Nacalai Tesque) at 4 °C for 10 min. After the beads were washed three times with PBS, proteins were eluted with 10 mM glutathione in 50 mM Tris-HCl buffer, pH 8.0. The samples were separated by SDS-PAGE. Protein bands were detected by Coomassie brilliant blue staining or western blotting with anti-Atg1 antibody. Signals were detected with an Immobilon (Millipore) western blot with a LAS4000 mini bioimaging analyzer (Fujifilm). For *in vitro* pulldown assay between GST–$Atg13^{17BR}$ and Atg17, the Atg31(174–196)-bound form of Atg17 was used because it markedly stabilized Atg17. Original images of gels and blots used in this study can be found in **Supplementary Figure 6**.

doi:10.1038/nsmb.2822

Isothermal titration calorimetry analysis. The binding of $Atg1^{tMIT}$ to $Atg13^{MIM}$ and $Atg13^{17BR}$ to Atg17 was measured by ITC, with a MicroCal iTC200 calorimeter (GE Healthcare), with stirring at 1,000 r.p.m. at 25 °C. The titration of $Atg13^{MIM}$–GB1 with $Atg1^{tMIT}$ involved 18 injections of 2 μl of the $Atg13^{MIM}$-GB1 solution (~150 μM) at intervals of 150 s into a sample cell containing 200 μl of $Atg1^{tMIT}$ (~20 μM). The titration of the $Atg13^{17BR}$ with Atg31(174–196)-bound Atg17 involved 18 injections of 2 μl of the $Atg13^{17BR}$ solution (~240 μM) at intervals of 120 s into a sample cell containing 200 μl of Atg31(174–196)-bound Atg17 (~24 μM). Because little heat of dilution was observed by titration of the $Atg13^{MIM}$ solution into PBS, the raw titration data were analyzed with the MicroCal Origin 7.0 software to determine the enthalpy (ΔH), dissociation constant (K_d) and stoichiometry of binding (N). Thermal titration data were fit to a single-site binding model, and thermodynamic parameters ΔH and K_d were obtained by fitting to the model. As for $Atg13^{MIM}$ F468A in **Figure 2c**, data were fit with a fixed N value of 1. The error of each parameter shows the fitting error.

LC-MS/MS analysis. The proteins were excised from each gel, destained and digested in the gels with 12.5 ng/μL trypsin (Promega) in 50 mM ammonium bicarbonate overnight at 30 °C. The phosphopeptides were enriched with Titansphere TiO beads (GL Sciences). LC-MS/MS analysis was performed on a LTQ Orbitrap Velos hybrid mass spectrometer (Thermo Fisher Scientific), with Xcalibur version 2.0.7, and coupled to an UltiMate 3000 LC system (Dionex, LC Packings). Label-free protein relative quantification was performed in Progenesis LC-MS (version 4.1, Nonlinear Dynamics). To identify the sequence of the yeast Atg13, peak lists were created with Progenesis LC-MS and searched against the *S. cerevisiae* protein sequences in the UniProt/SwissProt database (version January, 2013; 7,798 sequences) with Mascot (v2.4.1, Matrix Science). The search parameters were as follows: trypsin digestion with two missed cleavage permitted; variable modifications, protein N-terminal acetylation, oxidation of methionine, propionamidation of cysteine and phosphorylation of serine, threonine and tyrosine; peptide charge (2+, 3+ and 4+); peptide mass tolerance for MS data, ± 5 p.p.m.; and fragment mass tolerance, ± 0.5 Da.

Yeast strains and media. *S. cerevisiae* strains used in this study are listed in **Supplementary Table 3**. Standard protocols were used for yeast manipulation[38]. Cells were cultured at 30 °C in SD+CA medium (0.17% yeast nitrogen base without amino acids and ammonium sulfate, 0.5% ammonium sulfate, 0.5% casamino acids, and 2% glucose) supplemented with appropriate nutrients. Autophagy was induced by transferring the cells to SD(−N) medium (0.17% yeast nitrogen base, without amino acids and ammonium sulfate, and 2% glucose). Otherwise, to induce autophagy cells were treated with 0.2 μg/ml rapamycin (Sigma-Aldrich).

Cells expressing GFP- and mCherry- tagged proteins with a 17-residue linker (GGAAGGSSASGASGASG) were generated with the pYM series[39] with minor modification by a PCR-based gene-modification method[39]. Gene deletions were performed with pFA6a-kanMX6 series as described previously[39].

Antibodies. Anti-HA antibody (clone, 3F10) purchased from Roche was used for western blots at 1:5,000 dilution. Anti-GFP antibody (clone, 7.1/13.1) purchased from Roche was used for western blots at 1:1,000 dilution. Anti-Pgk1 antibody (cat. no. 459250) purchased from Invitrogen was used for western blots at 1:5,000 dilution. Anti-Atg1, anti-Atg13, anti-Atg17 and anti-Ape1 antibodies were described previously[7,9,40] and were used for western blots at 1:1,000 dilution, 1:1,000 dilution, 1:5,000 dilution, and 1:5,000 dilution, respectively. Rabbit polyclonal antibodies recognizing phosphorylated Ser428/Ser429 of Atg13 were produced by Sigma-Genosys against synthetic peptides KYS-pS-pS-FGNIRRH (residues 425–436) and used for western blots at 1:1,000 dilution. Validation for purchased antibodies is provided on the manufacturers' websites.

Immunoprecipitation. For the coimmunoprecipitation assay to examine the Atg1-Atg13 interaction, cells expressing Atg1-GFP were grown to mid-log phase (OD_{600} = 1.6–2.0) at 30 °C, and were treated or nor with rapamycin for 1 h before harvest. Cells harvested by centrifugation were washed twice with wash buffer (50 mM Tris-HCl, pH 8.0, 150 mM NaCl, 50 mM NaF, 5 mM EDTA, 5 mM EGTA, and 10% glycerol) and suspended in IP buffer (50 mM Tris-HCl, pH 8.0, 150 mM NaCl, 50 mM NaF, 5 mM EDTA, 5 mM EGTA, 10% glycerol, 500 nM microcystin (Wako), 1 mM PMSF (Sigma), 1× protease inhibitor cocktail for mammal (Sigma), and 1× PhosSTOP (Roche)), and lysed with 0.5 mm YZB zirconia beads (Yasui Kikai) and a Multi-Beads Shocker (Yasui Kikai) for 4 × 30 s. IP buffer containing 0.4% *n*-dodecyl-β-D-maltoside was added to the lysates, and the samples were rotated at 4 °C for 30 min. The solubilized lysates were cleared at 500*g* for 5 min at 4 °C, and resulting supernatant was subjected to a high-speed centrifugation at 17,400*g* for 15 min. The cleared supernatant was incubated with preequilibrated GFP-TRAP_M beads (Chromo Tek) and rotated at 4 °C for 1 h. After the beads were washed with wash buffer containing 0.2% *n*-dodecyl-β-D-maltoside, the bound proteins were eluted by incubation of the beads in SDS sample buffer (75 mM Tris-HCl, pH 7.5, 2% (w/v) SDS, 30% (v/v) glycerol, and 50 mM DTT) at 65 °C for 5 min and then subjected to immunoblotting with anti-Atg1 and anti-Atg13.

The Atg13-Atg17 interaction was examined in a similar manner as the Atg1-Atg13 interaction with some modifications. Cells expressing Atg13–2× HA were collected by centrifugation and were washed with PBS wash buffer (1× PBS, 50 mM NaF, 1 mM EDTA and 1 mM EGTA). Cells were lysed in PBS IP buffer (1× PBS, 50 mM NaF, 1 mM EDTA, 1 mM EGTA, 500 nM microcystin (Wako), 1 mM PMSF (Sigma), 1× protease inhibitor cocktail for mammal (Sigma), and 1× PhosSTOP (Roche)) as above. The lysates were solubilized with 1.0% Tween 20. After centrifugation, the cleared supernatant was incubated with preequilibrated anti-HA–conjugated agarose beads (Sigma) and rotated at 4 °C for 4 h. The bound proteins were eluted by incubation of the beads in SDS sample buffer at 65 °C for 5 min.

For analysis of the phosphorylation status of Ser428 and Ser429 in Atg13, Atg13–2× HA was immunoisolated from cell lysate in a similar experiment to examine the Atg13-Atg17 interaction. Cells expressing Atg13–2× HA were grown to mid-log phase (OD_{600} = 1.6–2.0) at 30 °C and were treated or not with rapamycin for 1 h or were starved by nitrogen-starvation medium for 1 h before harvest. Cells were collected by centrifugation and were washed with PBS wash buffer. Cells were also lysed in PBS IP buffer as above. The lysates were solubilized with 1.0% Triton X-100. After centrifugation, the cleared supernatant was incubated with preequilibrated PureProteome Protein G magnetic beads (Merck Millipore) and anti-HA (16B12; Covance). After rotation at 4 °C for 2 h, the bound proteins were eluted in SDS sample buffer at 65 °C 5 min.

Fluorescence microscopy. Fluorescence microscopy was performed at room temperature with an inverted fluorescence microscope (IX81, Olympus) equipped with an electron-multiplying CCD camera (ImagEM, C9100-13, Hamamatsu Photonics) and a 150× TIRF objective (UAPON 150XOTIRF, NA/1.45, Olympus). A 488-nm blue laser (50 mW, Coherent) and a 561-nm yellow laser (50 mW, Coherent) were used for excitation of GFP and mCherry, respectively. To increase image intensity and decrease background intensity, specimens were illuminated with a highly inclined laser beam[41]. For simultaneous observation of GFP and mCherry, both lasers were combined and guided without an excitation filter. Fluorescence was filtered with a Di01-R488/561-25 dichroic mirror (Semrock) and an Em01-R488/568-25 band-pass filter (Semrock) and separated into two channels with a U-SIP splitter (Olympus) equipped with a DM565HQ dichroic mirror (Olympus). The fluorescence was further filtered with an FF02-525/50-25 band-pass filter (Semrock) for the GFP channel and an FF01-624/40-25 band-pass filter (Semrock) for the mCherry channel. Images were acquired and processed by MetaMorph (Molecular Devices).

30. Sikorski, R.S. & Hieter, P. A system of shuttle vectors and yeast host strains designed for efficient manipulation of DNA in *Saccharomyces cerevisiae*. *Genetics* **122**, 19–27 (1989).
31. Otwinowski, Z. & Minor, W. *Methods Enzymol.* **276**, 307–326 (1997).
32. Adams, P.D. *et al.* PHENIX: a comprehensive Python-based system for macromolecular structure solution. *Acta Crystallogr. D Biol. Crystallogr.* **66**, 213–221 (2010).
33. Vagin, A. & Teplyakov, A. MOLREP: an automated program for molecular replacement. *J. Appl. Crystallogr.* **30**, 1022–1025 (1997).

34. Winn, M.D. *et al.* Overview of the CCP4 suite and current developments. *Acta Crystallogr. D Biol. Crystallogr.* **67**, 235–242 (2011).
35. Emsley, P., Lohkamp, B., Scott, W.G. & Cowtan, K. Features and development of Coot. *Acta Crystallogr. D Biol. Crystallogr.* **66**, 486–501 (2010).
36. Brünger, A.T. *et al.* Crystallography & NMR system: a new software suite for macromolecular structure determination. *Acta Crystallogr. D Biol. Crystallogr.* **54**, 905–921 (1998).
37. Murshudov, G.N., Vagin, A.A. & Dodson, E.J. Refinement of macromolecular structures by the maximum-likelihood method. *Acta Crystallogr. D Biol. Crystallogr.* **53**, 240–255 (1997).
38. Kaiser, C., Michaelis, S. & Mitchell, A. *Methods in Yeast Genetics: a Cold Spring Harbor Laboratory Course Manual* (Cold Spring Harbor Laboratory Press, 1994).
39. Janke, C. *et al.* A versatile toolbox for PCR-based tagging of yeast genes: new fluorescent proteins, more markers and promoter substitution cassettes. *Yeast* **21**, 947–962 (2004).
40. Suzuki, K., Morimoto, M., Kondo, C. & Ohsumi, Y. Selective autophagy regulates insertional mutagenesis by the Ty1 retrotransposon in *Saccharomyces cerevisiae*. *Dev. Cell* **21**, 358–365 (2011).
41. Tokunaga, M., Imamoto, N. & Sakata-Sogawa, K. Highly inclined thin illumination enables clear single-molecule imaging in cells. *Nat. Methods* **5**, 159–161 (2008).

doi:10.1038/nsmb.2822

nature COMMUNICATIONS

ARTICLE

Received 24 Sep 2013 | Accepted 4 Mar 2014 | Published 10 Apr 2014

DOI: 10.1038/ncomms4566

Nucleic acid sensing by T cells initiates Th2 cell differentiation

Takayuki Imanishi[1], Chitose Ishihara[1], Mohamed El Sherif Gadelhaq Badr[1], Akiko Hashimoto-Tane[1], Yayoi Kimura[2], Taro Kawai[3,†], Osamu Takeuchi[3,†], Ken J. Ishii[4,5], Shun'ichiro Taniguchi[6], Tetsuo Noda[7], Hisashi Hirano[2], Frank Brombacher[8], Glen N. Barber[9], Shizuo Akira[3] & Takashi Saito[1,10]

While T-cell responses are directly modulated by Toll-like receptor (TLR) ligands, the mechanism and physiological function of nucleic acids (NAs)-mediated T cell costimulation remains unclear. Here we show that unlike in innate cells, T-cell costimulation is induced even by non-CpG DNA and by self-DNA, which is released from dead cells and complexes with antimicrobial peptides or histones. Such NA complexes are internalized by T cells and induce costimulatory responses independently of known NA sensors, including TLRs, RIG-I-like receptors (RLRs), inflammasomes and STING-dependent cytosolic DNA sensors. Such NA-mediated costimulation crucially induces Th2 differentiation by suppressing T-bet expression, followed by the induction of GATA-3 and Th2 cytokines. These findings unveil the function of NA sensing by T cells to trigger and amplify allergic inflammation.

[1] Laboratory for Cell Signaling, RCAI, RIKEN Center for Integrative Medical Sciences (IMS-RCAI), Yokohama, Kanagawa 230-0045, Japan. [2] Graduate School of Medical Life Sciences, Yokohama City University, Yokohama, Kanagawa 236-0004, Japan. [3] Laboratory of Host Defense, WPI Immunology Frontier Research Center, Osaka University, Suita, Osaka 565-0871, Japan. [4] Laboratory of Adjuvant Innovation, National Institute of Biomedical Innovation, Ibaraki, Osaka 567-0085, Japan. [5] Laboratories of Vaccine Science, WPI Immunology Frontier Research, Osaka University, Suita, Osaka 565-0871, Japan. [6] Department of Molecular Oncology, Institute of Pathogenesis and Disease Prevention, Shinshu University Graduate School of Medicine, Matsumoto, Nagano 390-8621, Japan. [7] Department of Cell Biology, Cancer Research Institute of the Japanese Foundation of Cancer Research, Toshima-ku, Tokyo 170-8455, Japan. [8] International Center for Genetic Engineering and Biotechnology, Cape Town Component and Institute of Infectious Diseases and Molecular Medicine, Faculty of Health Science, Division of Immunology, University of Cape Town, Cape Town, South Africa. [9] Department of Cell Biology and the Sylvester Comprehensive Cancer Center, University of Miami Miller School of Medicine, Miami, Florida 33136, USA. [10] Laboratory for Cell Signaling, WPI Immunology Frontier Research Center, Osaka University, Suita, Osaka 565-0871, Japan. † Present addresses: Laboratory of Molecular Immunobiology, Graduate School of Biological Sciences, Nara Institute of Science and Technology (NAIST), Ikoma, Nara 630-0192, Japan (T.K.); Laboratory of Infection and Prevention, Institute for Virus Research, Kyoto University, Sakyo-ku, Kyoto 606-8507, Japan (O.T.). Correspondence and requests for materials should be addressed to T.S. (email: saito@rcai.riken.jp).

Toll-like receptors (TLRs) sense pathogen-associated molecular patterns to initiate not only innate responses but also to help regulate T cell-mediated adaptive immune responses[1,2]. While some TLRs are expressed on the cell surface, NA-sensing TLRs such as TLR3, TLR7/8 and TLR9 are expressed in endosomal compartments, allowing specific recognition of endocytosed pathogens.

Recent studies have shown that T cells also express TLRs and that TLR ligands can directly modulate T-cell responses. For example, TLR2 ligands directly promote proliferation of activated T cells[3,4], modulate the proliferation and suppressive functions of $CD4^+CD25^+$ regulatory T cells[5,6], trigger Th1 effector functions independently of TCR stimulation[7] and modulate Th17 responses[8].

In addition, it has been reported that ligands for NA-sensing TLRs enhance IL-2 production and proliferation of anti-CD3 antibody (Ab)-stimulated T cells[9,10] and promote survival of activated T cells[11], and further that the TLR8 ligand inhibits the suppressive function of regulatory T cells[12]. However, except for TLR2, very little is known about the molecular basis of the NA-sensing mechanisms and the functional consequences of NA-mediated costimulation in T cells.

Naive $CD4^+$ T cells differentiate into various effector T helper (Th) cells such as Th1, Th2 and Th17 cells, which produce IFN-γ, IL-4/IL-5/IL-9/IL-13 and IL-17/IL-22, respectively[13]. While Th1 and Th17 cells exhibit protective functions against intracellular pathogens and extracellular bacteria/fungi, Th2 cells protect from helminthic infection. Contrary to these protective functions, the same Th subsets can play a role in disease pathogenesis: Th1 for inflammatory diseases, Th2 for allergic diseases and Th17 for autoimmune diseases. While TLR stimulation of antigen-presenting cells (APCs) results in the production of IL-12, which induces Th1 differentiation, Th2 development is induced by IL-4, but the cells responsible for the initial wave of IL-4 production needed to induce Th2 differentiation remain elusive[14].

In this study, we report that NA-induced costimulatory responses of $CD4^+$ T cells are mediated independently of known NA sensors in innate immunity. We found that T cells take up NAs to induce costimulation and that the NA-mediated costimulation requires higher-order structure of the NAs by forming complexes with the antimicrobial peptides or with core histones. More importantly, costimulation of naive $CD4^+$ T cell with NAs induces Th2 differentiation through the downregulation of T-bet and the upregulation of GATA-3 expression. Thus, NAs directly induce T-cell costimulation through a unique NA-sensing mechanism to trigger the initial IL-4 production for Th2 differentiation, which might be involved in triggering and amplification of allergic inflammation.

Results

TLR-independent NA-mediated costimulation of $CD4^+$ T cells. To elucidate the functional significance of NA stimulation, naive $CD4^+$ T cells were stimulated with each TLR ligand. While none of the TLR ligands alone were able to induce cell proliferation or IL-2 production, proliferation and IL-2 production were selectively enhanced by Pam3 (TLR1/2), MALP-2 (TLR2/6), poly(I:C) (TLR3) and CpG-B (TLR9) with anti-CD3 stimulation (Fig. 1a).

We next determined whether this response is mediated by TLRs using mice deficient in both MyD88 and TRIF, which lack the capacity to respond to any of the known TLR ligands. Surprisingly, both poly(I:C) and CpG-B-mediated costimulation were normal in the MyD88/TRIF-doubly deficient $CD4^+$ T cells, whereas MALP-2 (TLR2)-mediated costimulation was completely abrogated (Fig. 1b), demonstrating that poly(I:C) and CpG-B-mediated T-cell costimulation was induced independently of TLR signaling.

Notably, DNA lacking CpG motifs required for TLR9 activation, such as non-CpG oligodeoxynucleotide (ODN) and DNA encoding GFP (GFP-S and GFP-AS, antisense strand) could also induce costimulation for IL-2 production (Fig. 1c). These data indicate that DNA induces T-cell costimulation independently of the CpG motifs. We also found that poly(dA), poly(dC) and poly(dG) but not poly(dT) induced the costimulation for IL-2 production, although the uptake of poly(dT) and non-CpG ODN by T cells was comparable (Fig. 1d).

Confocal microscopy analysis revealed that non-CpG ODN colocalized with an endosomal marker dextran and a lysosomal marker LysoTracker (Fig. 1e), indicating that non-CpG ODN is taken up by T cells and transported to endosomes/lysosomes, similarly in innate cells, and induces costimulatory signals in a TLR-independent manner.

Higher-order structure of NA induces T-cell costimulation. It is noteworthy that CpG-A possessing a poly(dG)-tail induced stronger costimulation of $CD4^+$ T cells than other ODNs such as CpG-B and non-CpG (Fig. 1c). The importance of the poly(dG) tract was confirmed by the finding that control ODN GpC corresponding to CpG-A induces robust IL-2 production, similar to CpG-A (Fig. 2a), and that replacement of the poly(dG) motif of GpC by poly(dA), poly(dC) or poly(dT) resulted in the complete loss of stimulatory activity (Fig. 2b).

It has been reported that the poly(dG) tail induces the spontaneous formation of large multimeric aggregates via G-quadruplex formation[15]. Indeed, when GpC was rendered single-stranded by heating and flash-cooling, a dramatic reduction of IL-2 production was observed (Fig. 2c), suggesting that higher-order structures mediated by the poly(dG) motif are critical for enhanced costimulation by CpG-A and GpC. Consistently, introduction of a poly(dG)-tail to non-CpG and CpG-B that possess a phosphodiester (PO) backbone sensitive to DNase enabled them to induce costimulation, whereas the same DNA without the poly(dG)-tail could not (Fig. 2d).

It has been shown that the poly(dG) motif not only protects against DNase degradation[16] but also enhances the cellular uptake of the ODN[17]. Indeed, the uptake of GpC-poly(dC) by T cells was lower than GpC, indicating that GpC-poly(dC) could not induce costimulation due to its poor uptake (Fig. 2e). It is noteworthy that cellular uptake of GpC-poly(dC) was weaker than that of non-CpG (Fig. 2e). It has been reported that phosphorothioate (PS)-modified ODN are taken up more efficiently than PO-ODN[17]. The entire backbone of non-CpG is PS, whereas it is only partial in GpC (Supplementary Table 1). PS modification of GpC-poly(dC) led to enhanced cellular uptake and costimulation (Fig. 2e). By contrast, modification of non-CpG to contain only partial PS resulted in decreased uptake and the failure of costimulation (Fig. 2e). We also confirmed that cellular uptake and costimulation of PO-backboned non-CpG was much weaker than those of PS-backboned non-CpG (Supplementary Fig. 1a). These data indicate that efficient uptake of DNA via its poly(dG) tail or PS modification is critical for induction of costimulation.

While inosine or guanine-containing RNA such as poly(I), poly(G), poly(I:C) and poly(C:G) could induce costimulation, poly(A), poly(U), poly(C) and poly(A:U) could not (Fig. 2f). The induction of costimulation by RNA was correlated with the cellular uptake of RNA (Fig. 2f). These data indicate that RNA-mediated costimulation depends on the RNA sequence for cellular uptake of RNA to induce costimulation.

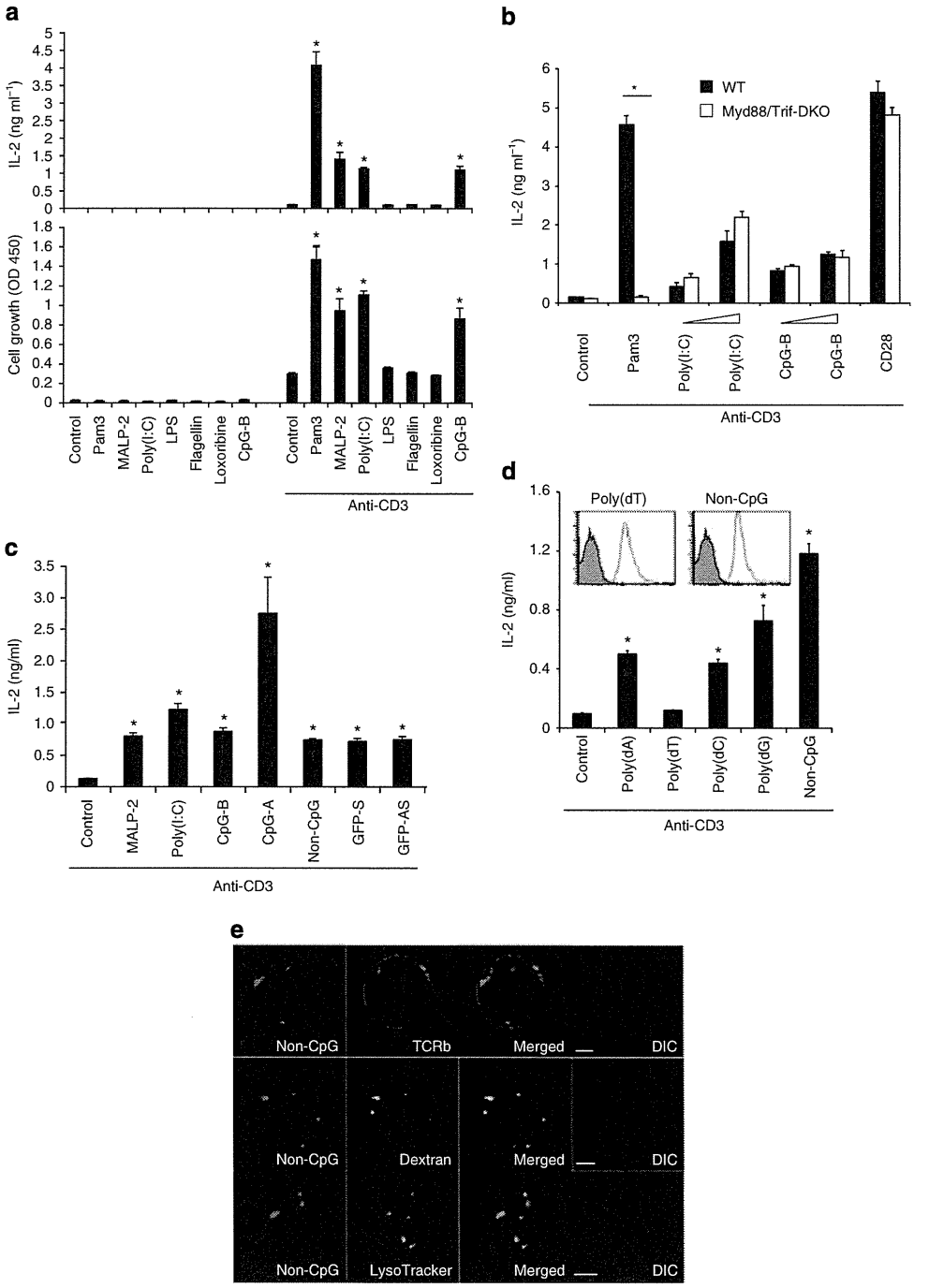

Figure 1 | DNA/RNAs are incorporated into and induce costimulation of CD4$^+$ T cells. (**a**) Naive CD4$^+$ T cells were cultured with indicated TLR ligands (Pam3: 5 μg ml^{-1}, MALP-2: 5 μg ml^{-1}, poly(I:C): 100 μg ml^{-1}, Flagellin: 1 μg ml^{-1}, Loxoribine: 100 μM, CpG-B: 5 μM) in the presence or absence of immobilized anti-CD3ε Ab (10 μg ml^{-1}). After 48-hour incubation, IL-2 production and cell growth were assessed by ELISA and MTS assay, respectively. *$P<0.05$, Student's *t*-test (compared with anti-CD3 alone). (**b**) Naive CD4$^+$ T cells from WT or *Myd88*$^{-/-}$*Trif*$^{-/-}$ mice were stimulated with the indicated TLR ligands or anti-CD28 (Clone: 37.51, 5 μg ml^{-1}) in the presence of immobilized anti-CD3ε Ab. *$P<0.05$, Student's *t*-test (compared with WT cells treated with Pam3). (**c**,**d**) Naive CD4$^+$ T cells were stimulated with the indicated NAs (**c**) and ODNs (**d**) in the presence of immobilized anti-CD3ε Ab. These T cells were incubated with the Cy5-labelled ODNs at 37 °C for 90 min and ODN uptake was determined by flow cytometry (**d**, upper). *$P<0.05$, Student's *t*-test (compared with anti-CD3 alone). (**e**) Naive CD4$^+$ T cells were incubated with 5 μM non-CpG-Cy5 for 90 min and dextran-Alexa Fluor 488 or LysoTracker for last 10 min for the subcellular staining of endosomes and lysosomes, respectively. Confocal microscopy data with differential interference contrast (DIC) images of representative cells are shown. Scale bars, 2.5 μm. Error bars indicate s.d. Data are representative of at least three independent experiments.

It has been reported that poly(I) forms parallel four-stranded helices held together by hydrogen-bonded inosine quartets, similar to poly(dG) chains[18]. We found that heat denaturation of poly(I:C) and poly(G) resulted in impaired costimulation (Fig. 2g), indicating that the ability of RNA to induce T-cell costimulation is dependent on the higher-order structure similar to DNA.

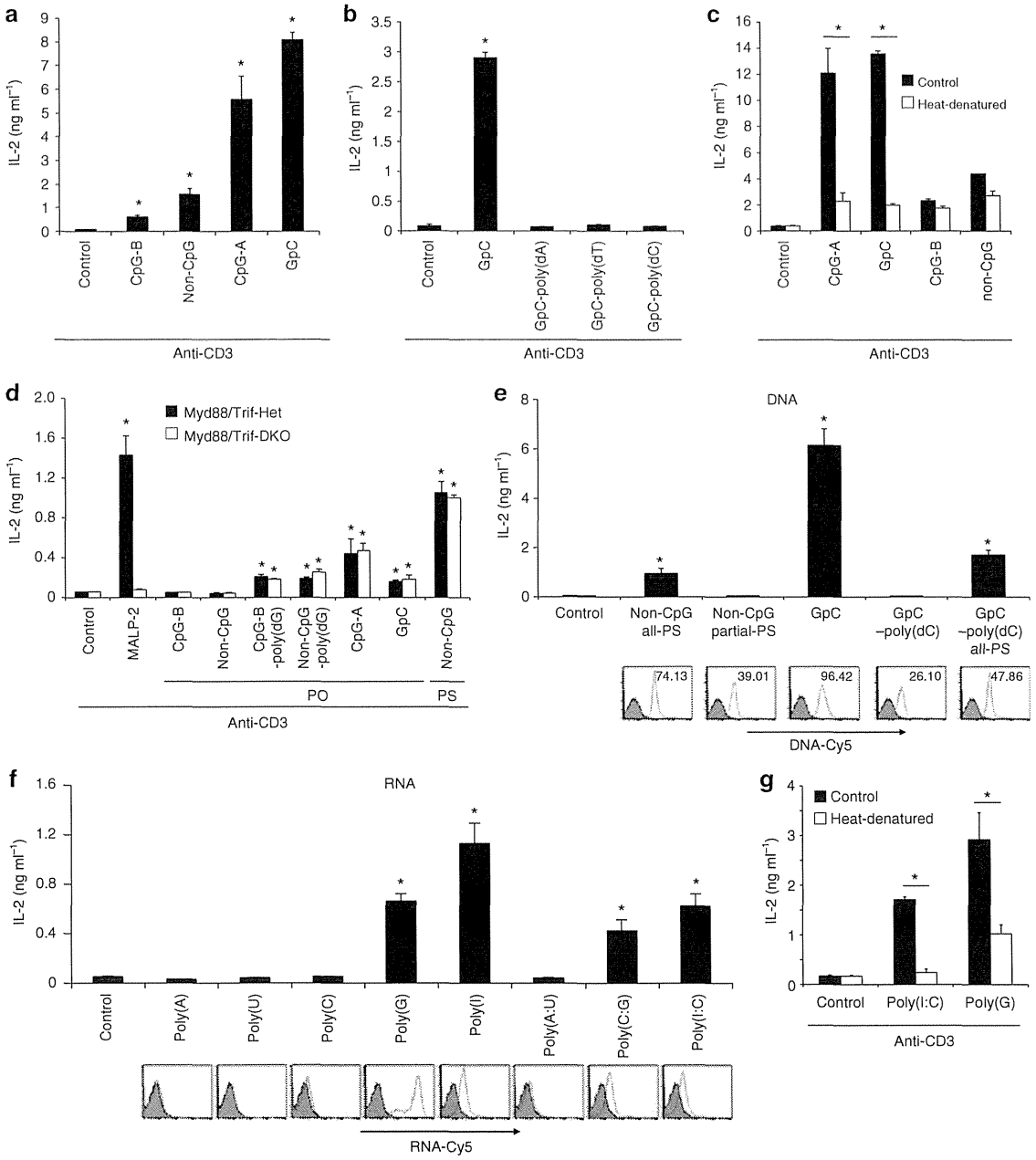

Figure 2 | Properties of DNA/RNAs required for T cell costimulatory activity. (**a**–**c**) Naive CD4$^+$ T cells were activated with plate-bound anti-CD3ε with various DNAs—*$P<0.05$, Student's *t*-test (compared with anti-CD3 alone) (**a**); GpC with different poly tails. *$P<0.05$, Student's *t*-test (compared with anti-CD3 alone) (**b**); and heat-denatured ODNs. *$P<0.01$, Student's *t*-test (compared with the untreated control) (**c**). After 48 h, IL-2 production was measured by ELISA. (**d**) Naive CD4$^+$ T cells derived from *Myd88*$^{+/-}$ *Trif*$^{+/-}$ and *Myd88*$^{-/-}$ *Trif*$^{-/-}$ mice were activated with immobilized anti-CD3ε together with the indicated DNAs. *$P<0.05$, Student's *t*-test (compared with anti-CD3 alone in WT cells). (**e**) Naive CD4$^+$ T cells were stimulated with immobilized anti-CD3ε together with all (all-PS) or partially (partial-PS) PS-modified ODN. CD4$^+$ T cells were incubated with the Cy5-labelled ODN at 37 °C for 90 min, washed and analysed for incorporated ODN by flow cytometry (bottom panels). *$P<0.05$, Student's *t*-test (compared with anti-CD3 alone). (**f**) Naive CD4$^+$ T cells were stimulated with indicated ODNs and analysed similarly as in (**e**). *$P<0.05$, Student's *t*-test (compared with anti-CD3 alone). (**g**) Naive CD4$^+$ T cells were stimulated and analysed similarly in (**c**). *$P<0.05$, Student's *t*-test (compared with the untreated control). Error bars indicate s.d. Data are representative of at least three independent experiments.

Costimulation induced by NA complexed with LL37 and histones. It has been recently shown that endogenous self-DNAs stimulate plasmacytoid dendritic cells by forming aggregated structures upon binding with the antimicrobial peptide LL37 (ref. 19). Similarly, we found that mammalian and bacterial genomic DNA were taken up by T cells and induced costimulation when mixed with LL37 while they alone were neither incorporated nor induce stimulation (Supplementary Fig. 2a, Fig. 3a). Similarly, although poly(A) and poly(A:U) *per se* were defective in cellular uptake and induction of costimulation of naive CD4$^+$ T cells (Fig. 2f), they were incorporated and induced T-cell costimulation when complexed with LL37 (Supplementary Fig. 2b, Fig. 3b).

Similar to LL37, extracellular histones as components of neutrophil extracellular traps exhibit antimicrobial function[20]. We found that the addition of core histones (H2A, H2B, H3 and

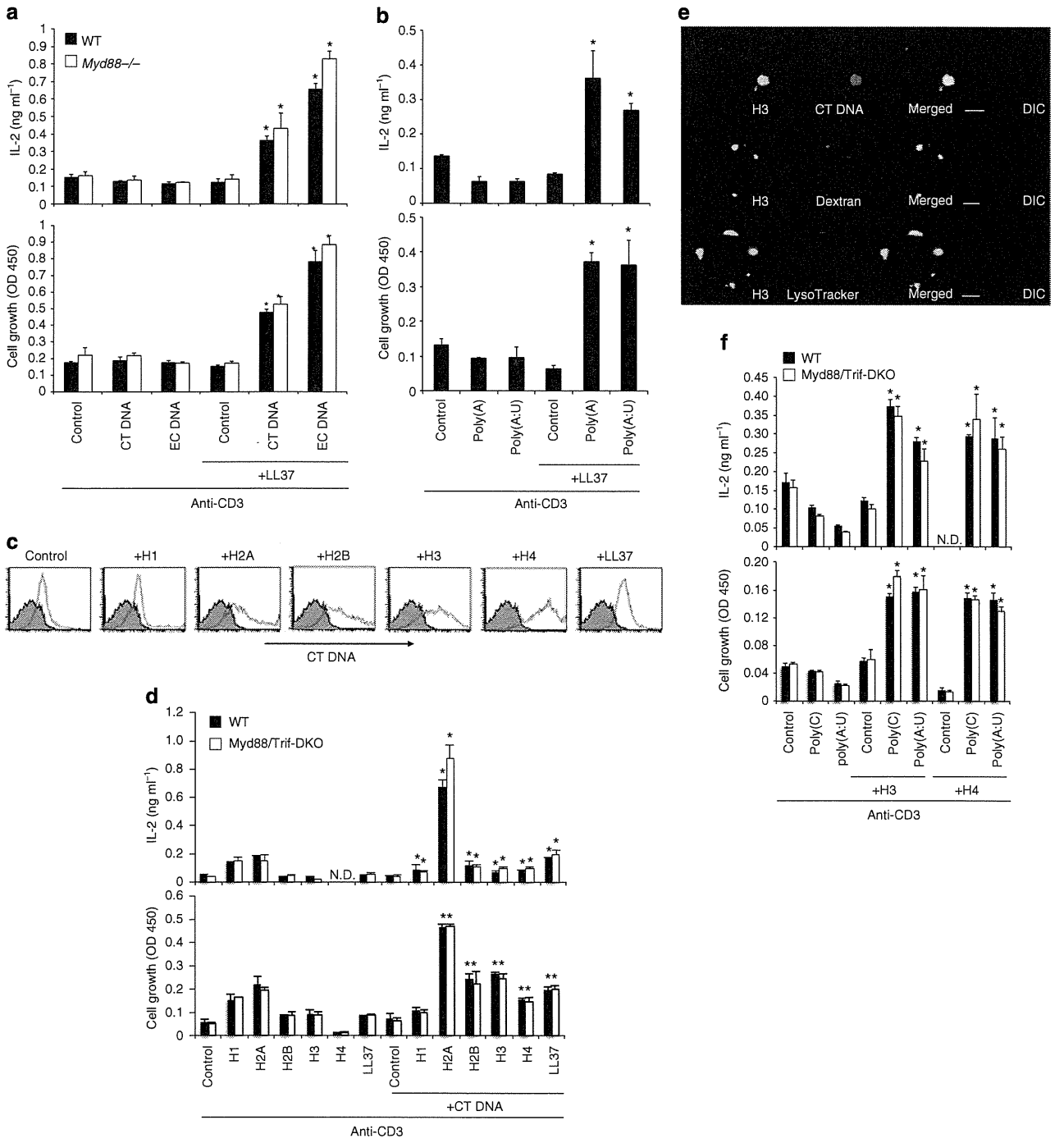

Figure 3 | T-cell activation by NAs complexed with antimicrobial peptides or core histones. (**a**,**b**) Naive CD4$^+$ T cells derived from WT and *Myd88*$^{-/-}$ mice were stimulated with plate-bound anti-CD3ε together with calf thymus (CT)- or *E. coli* (EC)-derived genomic DNA (**a**) or RNAs (**b**) either alone or premixed with LL37. After 48 h, IL-2 production and cell growth were assessed by ELISA and MTS assay, respectively. *$P<0.05$, Student's *t*-test (compared with anti-CD3 plus LL37 in WT cells). (**c**) Naive CD4$^+$ T cells were incubated with the Cy5-labelled CT DNA premixed with the indicated histones or LL37 at 37 °C for 90 min and the incorporated DNA were analysed by flow cytometry. (**d**,**f**) Naive CD4$^+$ T cells derived from WT and *Myd88*$^{-/-}$ *Trif*$^{-/-}$ mice were stimulated with plate-bound anti-CD3 together with CT DNA alone (**d**), RNAs alone (**f**) or premixed with various histones (**d**,**f**), and analysed similarly in (**a**). *$P<0.05$, Student's *t*-test (compared with anti-CD3 plus each histone or LL37 in WT cells). (**e**) Naive CD4$^+$ T cells were stimulated with anti-CD3 with Cy5-labelled CT DNA premixed with Alexa488-labelled histone H3 for 18 h. Endosomes and Lysosomes were visualized by staining with dextran-Alexa Fluor 488 and LysoTracker, respectively. Confocal and differential interference contrast (DIC) images of representative cells are shown. Scale bars, 2.5 μm. Error bars indicate s.d. Data are representative of at least two independent experiments.

H4), but not the linker histone H1, increase cellular uptake of genomic DNA into CD4$^+$ T cells (Fig. 3c). The uptake was correlated with induction of costimulation (Fig. 3d). Although the genomic DNA–H2A complex was the strongest inducer for IL-2 production, H2A itself induces costimulation in the absence of DNA through unknown mechanism. Therefore, we use H3 that has no costimulatory activity by itself to determine the localization of histone/DNA complexes. The genomic